THE ASTROPHYSICAL JOURNAL SUPPLEMENT SERIES, 74:1129–1149, 1990 December

FREQUENCIES OF SOLAR OSCILLATIONS

K. G. LIBBRECHT,[1] M. F. WOODARD, AND J. M. KAUFMAN[2]
Big Bear Solar Observatory, California Institute of Technology
Received 1989 December 20; accepted 1990 April 27

ABSTRACT

We observed solar oscillations at different spatial scales using three different data sets acquired at Big Bear Solar Observatory during 1986–1987. Using these data, we present a new and more accurate table of the Sun's oscillation mode frequencies, ν_{nl}, as a function of radial order n and spherical harmonic degree l. These frequencies are averages over azimuthal order m and therefore approximate the normal mode frequencies of a nonrotating, spherically symmetric Sun, near solar minimum. After including some results from other workers for completeness, the table presented here contains frequencies for most of the solar p- and f-modes with $0 \leq l \leq 1860$, $0 \leq n \leq 26$, and $1.0 \leq \nu_{nl} \leq 5.3$ mHz. Frequency uncertainties, σ_{nl}, for individual multiplets are in some cases as low as 10 nHz, and the combined frequency uncertainty for the entire set is given by $(\sum_{nl} \sigma_{nl}^{-2})^{-1/2} \approx 700$ pHz. Comparing the f-mode ridge with the theoretically expected frequencies, $\omega^2 = gk_h$, we find that the observed frequencies are significantly less than expected for $l > 1000$, for which we have no explanation.

Subject headings: Sun: oscillations

I. INTRODUCTION

Helioseismology is the study of the oscillations of the Sun, especially with the goal of determining the structure and dynamics of the unseen solar interior by careful measurements of the spectrum of solar oscillations. Possible oscillation modes that can exist on the Sun are those for which the restoring force is primarily pressure (p-modes), buoyancy (g-modes), the Coriolis force (inertia or r-modes), plus a class of surface or interface modes (f-modes). Of these, only p- and f-modes with periods around 5 minutes and spherical harmonic degrees l between 0 and $\sim$3000 have been definitely observed. These oscillations may be observed both as intensity fluctuations in the continuum and spectrum lines, and as Doppler shifts of spectrum lines. (For reviews of helioseismology see Vorontsov and Zharkov 1989; Libbrecht 1988*a*; Christensen-Dalsgaard, Gough, and Toomre 1985; Deubner and Gough 1984).

The solar normal mode frequencies, ν_{nl}, as a function of degree l (averaged over azimuthal order m) and radial order n, are particularly useful in modeling the radial structure of the Sun, since the agreement between the measured and calculated mode frequencies can be used to test solar models. Without the normal mode spectrum, one would have to be satisfied with reproducing little more than the observed solar radius and luminosity given the Sun's mass, age, and chemical composition —not a good situation given the uncertainties in the solar helium abundance and the physics of convection. Further, because different solar oscillation modes penetrate the solar interior to different depths, it is possible, with an accurate set of mode frequencies, to invert the data to determine the internal sound speed as a function of radius (Christensen-Dalsgaard 1988; Christensen-Dalsgaard *et al.* 1985). And from this one would hope that a better understanding of the physics of the solar interior would ensue.

[1] Alfred P. Sloan Research Fellow.
[2] NASA Graduate Student Researchers Program Fellow.

With this in mind, we have undertaken to produce a new set of solar oscillation mode frequencies, with as high an accuracy as possible and covering the greatest range in l and ν possible; our results are presented in Table 1 at the end of this paper. This work is based on, and is an extension of, a previous set of frequencies described by Duvall *et al.* (1988) and Libbrecht and Kaufman (1988). The present table, using new and better data, contains a greater range in l and ν, plus frequency uncertainties and systematic errors that are considerably smaller than those quoted in these previous papers.

II. MODE PHYSICS AND DATA ANALYSIS

At low l and n, the Sun's p-mode spectrum consists of a large number of globally coherent modes, each identified by quantum numbers n, l, and m. The f-modes are conveniently labeled as an extension of the p-mode spectrum with $n = 0$ (see Deubner and Gough 1984). A standard practice which we have used below for identifying individual solar normal modes is to fit a time series of solar images (either brightness or Doppler images) to projected spherical harmonics with a range of l and m, and then Fourier-transform the time series of fit coefficients. The resulting power spectra, $S_{lm}(\nu)$, show a number of sharp features due to solar p- and f-modes, and these power spectra are further analyzed to determine the solar oscillation frequencies. Because of our inability to see instantaneously the entire surface of the Sun, our observational resolution in l and m is no smaller than approximately 3, and, of course, we have no intrinsic resolution in n, since our observations are of only the solar surface. The mode frequency separation in n, $\partial\nu_{nlm}/\partial n$, at fixed l and m, is fortunately quite large, so that modes with identical l and m but different n are easily resolved in the $S_{lm}(\nu)$ power spectra. The frequency separation of modes with fixed n and m and different l is considerably smaller, very roughly $\partial\nu_{nlm}/\partial l \approx \nu_{nl}/2l$, and for modes with constant n and l and different m we have $\partial\nu_{nlm}/\partial m \approx 0.4\ \mu$Hz, the latter splitting caused primarily by solar rotation.

For low-l modes (by which we mean $l \lesssim 100$) the mode line width, Γ, is a strong function of ν (Libbrecht 1988*b*; Elsworth *et al.* 1988), and only for the very lowest frequency modes currently observed are we able to resolve the $\Delta m = \pm 2$ sidelobes from a central (n, l, m) peak (which occurs at low l for p-modes with frequencies below ~ 1.8 mHz; Libbrecht 1988*b*). Thus, for most of the p-modes we observe at low l, the information we glean comes from power spectral peaks which include power from at least several different azimuthal modes.

Another standard practice that we have employed in the current data analysis to increase our signal-to-noise ratio is to average power spectra over all m for a fixed l, forming averaged power spectra, $S_l(\nu)$, after first displacing the individual $S_{lm}(\nu)$ spectra to remove the rotational splitting. [See Libbrecht 1989 and Fig. 1 below for samples of raw power spectra, $S_{lm}(\nu)$, and averaged power spectra, $S_l(\nu)$, respectively.] The resulting multiplet peaks in the averaged power spectra are then analyzed to determine the frequencies of the p-modes at fixed l and n, which approximate what one would find if the Sun were spherically symmetric.

For most of the observed p-modes with $l \lesssim 60$ and $\nu_{nl} \lesssim 4$ mHz, the multiplet peaks in the averaged power spectra at fixed n and l do not overlap with one another or with temporal sidelobes, since Γ is relatively small and $\partial\nu_{nl}/\partial l > 11.6$ μHz. Such multiplets are nicely fitted by individual Lorentzian functions, and give a clean measure of the multiplet frequency that is largely free of any systematic errors, other than those present from the average over m. At slightly higher l or ν, however, the multiplet peaks do overlap somewhat, both with each other and with temporal sidelobes, and individual Lorentzians will no longer give an adequate fit. For such peaks it is necessary to model the data better, including spatial and temporal sidelobes, by fitting the power spectra with a set of overlapping Lorentzian functions. If done properly, this procedure will also produce multiplet frequencies that are free of systematic errors, at least down to the few nanohertz level.

At still higher l or ν, say for $l \gtrsim 250$ (the value here is not very well known) or $\nu_{nl} \gtrsim 4$–5 mHz, the mode line width is greater than $\partial\nu_{nl}/\partial l$, and therefore it is impossible to resolve individual multiplets even partially. Indeed, at this point the oscillations will no longer be true global modes. In principle, one could again make a detailed model of the data to determine a mean multiplet frequency, although the large widths of the spectral peaks for this range of l and ν make accurate frequency determinations more difficult. We have chosen here a somewhat simpler and quicker analysis, namely, to fit the constant-n features in the averaged power spectra (which appear as ridges in an l-ν power diagram) to Gaussian functions of ν, then using the centroid of the Gaussian to estimate the ridge frequency at fixed l (Libbrecht and Kaufman 1988).

These Gaussian "ridge fits" are not completely free of systematic error, however, since they do not derive from a detailed model of the data. In addition to a possible scale error in the images, the dominant source of systematic errors in ridge fit frequencies is due to a combination of the facts that our set of spatial filter functions is not completely orthogonal, and that the oscillation power, P, is not constant at fixed n. The former allows spatial sidelobes from modes with $l' \neq l$ to leak into the spectrum $S_l(\nu)$, while the latter ensures that sidelobes that are approximately symmetrically spaced in frequency about the central peak are not of equal amplitude. This tends to pull the measured frequency of a ridge in the direction of higher power. These systematic errors are approximated by

$$\Delta\nu \approx \frac{1}{2} s^2 \frac{d\nu}{dl} \frac{1}{P} \frac{\partial P(n, l)}{\partial l} + \epsilon l \frac{d\nu}{dl}$$
$$\approx \frac{1}{2} s^2 \left(\frac{d\nu}{dl}\right)^2 \frac{1}{P} \frac{\partial P(\nu, l)}{\partial \nu} + \frac{1}{2} s^2 \frac{d\nu}{dl} \frac{1}{P} \frac{\partial P(\nu, l)}{\partial l} + \epsilon l \frac{d\nu}{dl}, \tag{1}$$

where we have followed Libbrecht and Kaufman (1988) in approximating the spherical harmonic overlap function by $V(l, l') = \exp[-(l - l' - \alpha)^2/s^2]$, with $\alpha = \epsilon l$ representing a small scale error. While this correction is better than nothing, a comparison of Lorentzian peak fits and Gaussian ridge fits for the same modes shows that some systematic errors remain in the ridge fit data, although these become smaller as one goes to higher l-values.

Below we present three different oscillation data sets acquired at Big Bear Solar Observatory (BBSO): a low-resolution set consisting of full-disk solar Doppler images, an intermediate-resolution set consisting of full-disk Ca II K images, and a high-resolution set consisting of Doppler images covering the center tenth of the solar disk. Our analyses of these different data sets, presented in the following sections, proceeded along the following lines: (1) fit the solar images with projected spherical harmonics, and Fourier-transform the resulting fit coefficients; (2) average over m to form combined power spectra, after first correcting for the solar rotational splitting; (3) if the mode peaks are well resolved, fit with Lorentzian functions; if they are partially resolved, fit with a sum of Lorentzians; and if the modes are not at all resolved, use Gaussian ridge fits along with the correction in equation (1). Frequency uncertainties in the low-resolution data set were determined primarily from the Lorentzian fits themselves, and in the other two data sets the uncertainties were inferred by measuring the scatter in the fit frequencies along a given ridge. That is, for each l in a given ridge, a quadratic polynomial in l' was fitted to the frequencies in that ridge over some range $l - \Delta l \leq l' \leq l + \Delta l$. After subtracting the polynomial fit, the uncertainty was determined from the residual scatter, assuming normally distributed errors. The details of these procedures when applied to the present three data sets are discussed below.

III. THE LOW-RESOLUTION DATA SET

The observations which produced the low-resolution data shown here were made using the dedicated helioseismology telescope at BBSO. This telescope and its data acquisition system have already been described in some detail by Libbrecht and Zirin (1986) and Libbrecht (1988*b*). In essence, a Zeiss 0.25 Å birefringent filter in combination with a KD*P electro-optical crystal was used to produce full-disk solar images in the red and blue wings of the 6439 Å calcium line. By digitizing and differencing the images from the two wings of the line, solar Doppler images were produced at a rate of one per minute. The telescope was operated from 1986 March 26 to August 2, producing 100 days of useful data and nearly 60,000 full-disk solar Doppler images. The data were processed by fitting each image to all spherical harmonics with $l \leq 110$, and each m for all even l for $110 \leq l \leq 140$, using the technique described in Libbrecht and Zirin (1986). The fit coefficients were subsequently Fourier-transformed in time to produce power spectra for each l and m. The computations were performed largely at the San Diego Supercomputer Center using a CRAY X-MP. With this machine the computational burden was not tremendous, and the factors which limited the present analysis to $l \leq 140$ were the limited storage space available for the data and a desire to minimize the data transfer times. This same data set, but restricted to $l \leq 60$, was used to make very accurate measurements of p-mode amplitudes and line widths (Libbrecht 1988b), as well as p-mode frequency splittings (Libbrecht 1989).

In order to pick out individual p-mode multiplet frequencies from the data, power spectra for each m with a given l were added together, after first correcting for the frequency splitting, which greatly improves the signal-to-noise ratio (Libbrecht and Zirin 1986). The splitting here was approximated by fitting a_i^* from the previous analysis (Libbrecht 1989) to the functional form $a_i^*(l) \rightarrow A_i + B_i(l-60)^2$, using i between 1 and 5, then using the fit value at each l. We took $b_i^* = 0$, and above $l = 60$ the splitting was taken to be equal to the $l = 60$ value. Since the Legendre polynomials, $P_i(m/l)$, form a nearly orthogonal set between -1 and 1, correcting for the splitting with slightly incorrect values of the splitting parameters will not shift the measured multiplet frequency significantly. (Variations in the mode amplitudes with m could shift the centroid of the multiplet if an incorrect splitting correction is made, but we estimate that the shift will be random and at most a few nanohertz, and can be neglected for the present.)

Figure 1 shows a sample of the averaged power spectra that were obtained in this manner with the BBSO 1986 data set; the same plot was presented in Duvall *et al.* (1988), Figure 3a, using the shorter 1985 BBSO seismology data set. The features are the same as in the previous plot, but because of the longer run the signal-to-noise ratio is significantly higher. Note also that the mode line widths in Figure 1 are the result of the finite mode lifetimes, which are much shorter than the duration of the observations; lower frequency modes show much sharper features (Libbrecht 1988b).

After obtaining initial guesses for the mode frequencies, ν_{nl}, from the previous frequency tables and by extrapolating known ridges, sections of the averaged power spectra, $S_l(\nu)$, were fitted to Lorentzian functions,

$$S_l(\nu) \rightarrow \frac{A}{(\nu - \nu_{nl})^2 + \sigma^2} + B, \qquad (2)$$

by a nonlinear, least-squares fit, adjusting the parameters A, ν_{nl}, σ, and B. Uncertainties for the fitted quantities were determined from the fit, after first weighting the power spectra points in a way equivalent to assuming that the noise in the power spectrum was proportional to $S_l(\nu)$ (this gives the same uncertainties one obtains from a maximum-likelihood method, assuming that the spectrum is distributed as χ^2 with 2 degrees of freedom). We found that assuming such a weighting function in the initial least-squares fit gave poor results, since the "wings" of the spectral features were weighted too heavily. Hence uniform weighting was used for the fit, and the more realistic $S_l(\nu)$ weighting was used to estimate uncertainties.

This fitting procedure worked well for low-l, and low-ν modes, where the temporal and spatial sidelobes do not inter-

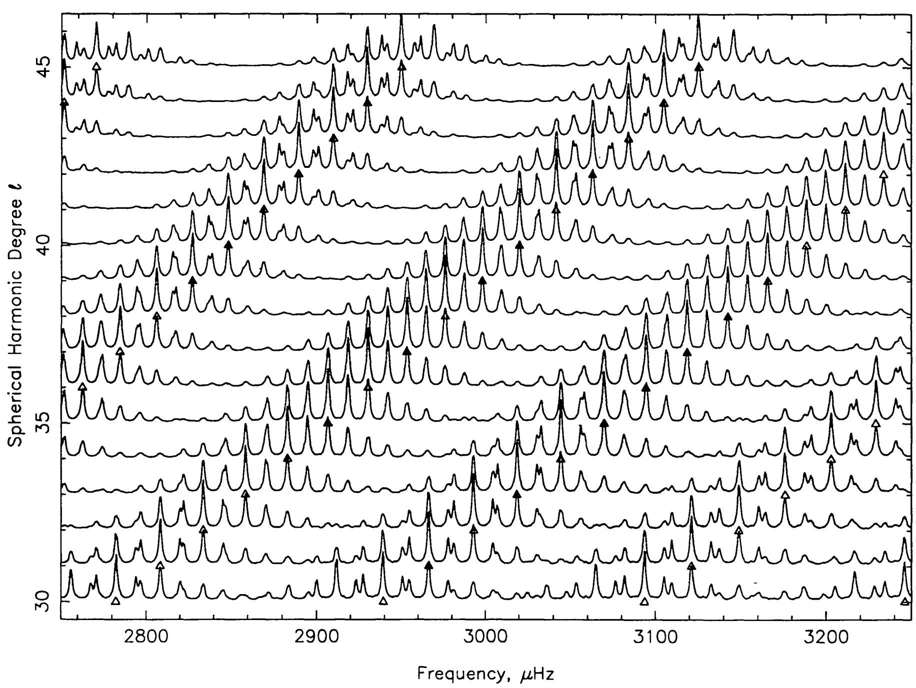

FIG. 1.—Sections of averaged power spectra from the low-l BBSO data set, with the solar p-mode frequencies marked by triangles below the multiplet peaks. Note that for each real solar peak there are a number of temporal and spatial sidelobes. This plot is essentially the same as that presented in Duvall *et al.* (1988, Fig. 3a), but the present data set shows a much higher signal-to-noise ratio.

fere with the multiplet peaks. But at higher l, particularly for $l \sim 100$, where $\partial \nu_{nl}/\partial l \approx 11.6$ μHz, a slightly different fitting function was used in order to avoid systematic errors arising from the contamination of the multiplet peaks with sidelobes. For these modes, sections of averaged power spectra were fitted to a sum of Lorentzians,

$$S_l(\nu) \rightarrow \sum_i \frac{AC_i}{(\nu - \nu_{nl} - \Delta\nu_i)^2 + (\sigma + \delta_i)^2} + B, \qquad (3)$$

again adjusting the four parameters A, ν_{nl}, σ, and B.

The C_i, $\Delta\nu_i$, and δ_i represent the relative amplitudes, frequency shifts, and line-width increases of all the nearby spatial and temporal sidelobes that might interfere with the multiplet peak of interest. In principle, with an accurate knowledge of the gain of the full-disk Doppler images across the solar disk, the C_i could be accurately calculated, since these are simply related to the cross-products of the projected spherical harmonics over the visible solar disk (as well as the relative amplitudes of the temporal sidelobes). For the present analysis, however, the C_i were measured at a few low-l values where the sidelobes did not interfere a great deal, and at a few high-l values using CLEANed data (Hogbom 1974), and the measured numbers were used to interpolate to other l-values. The $\Delta\nu_i$ were obtained from the measured mode frequencies to the necessary level of accuracy by fitting ν_{nl} on a given ridge to polynomials in l. For this the fit ν_{nl} were used, after an initial iteration using frequency estimates. The δ_i appear because of the averaging done to get the averaged spectra, $S_l(\nu)$; spatial sidelobes in $S_l(\nu)$ from modes with $l' \neq l$ appear broader than the l multiplets, because of the cross-products with different m (see Fig. 1). At low ν, where the natural mode line widths are small and all the structure can be seen (and we can use the simpler fit above), the character of the δ_i is clearly visible. Here an l multiplet appears in the $S_l(\nu)$ as a single central peak flanked by two "$m = \pm 2$" peaks (Libbrecht 1988*b*, Fig. 2), whereas the modes with $l' = l \pm 1$ appears as an "$m = \pm 1$" doublet separated by ~ 0.8 μHz. At higher frequencies this structure is adequately approximated by a simple increased line width, since the effect on the fit mode frequencies is small. As with the C_i, measured δ_i at a few l-values were used to interpolate to other l-values.

To check for systematic errors introduced by the above multiple Lorentzian fits, we compared fits using the above functional form with the simpler fits applied to power spectra, $S_l^*(\nu)$, which had been CLEANed to remove temporal sidelobes (see, e.g., Hogbom 1974). A comparison of multi-Lorentzian fits to $S_l(\nu)$ with simpler fits to $S_l^*(\nu)$, for the worst case around $l \sim 100$ showed frequency differences that were typically less than 50 nHz, with random sign. Thus from this test we expect that the systematic errors in the measured mode frequencies introduced by temporal and spatial sidelobes are no more than a few tens of nHz near $l \approx 100$, and completely negligible when $\partial \nu_{nl}/\partial l$ is not close to 11.6 μHz. CLEANing the power spectra works quite well to remove the effects of temporal sidelobes, as long as the mode features are fairly sharply peaked and the signal-to-noise ratio of the data is high. However because CLEANing did not do well at high ν, we chose to do the entire analysis on the unCLEANed data.

The above Lorentzian fitting procedures worked well over most of the l-ν plane, and produced the multiplet frequencies shown schematically in Figure 2. About a dozen of the very

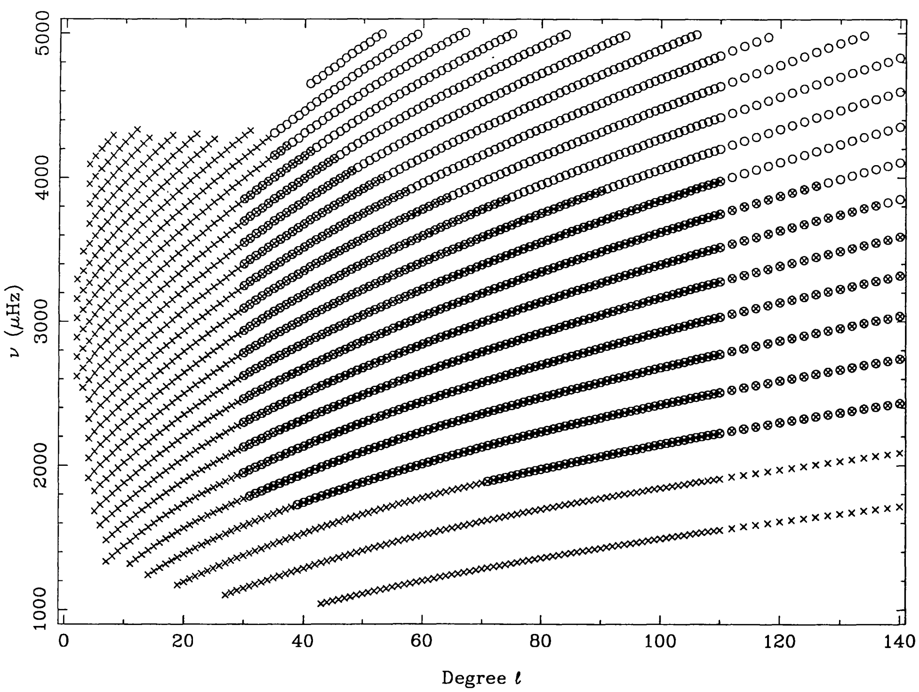

FIG. 2.—Schematic l-ν diagram, showing the mode frequencies from the Lorentzian fits (*crosses*), along with mode frequencies determined from the less precise "Gaussian ridge fitting" procedure (*open circles*), after correcting for known systematic errors. The ridge fit frequencies serve to fill in the l-ν diagram at high ν, but a comparison of the ridge fits with the more accurate Lorentzian peak fits shows that the ridge fits at these low l-values still contain systematic errors at the 1–2 μHz level.

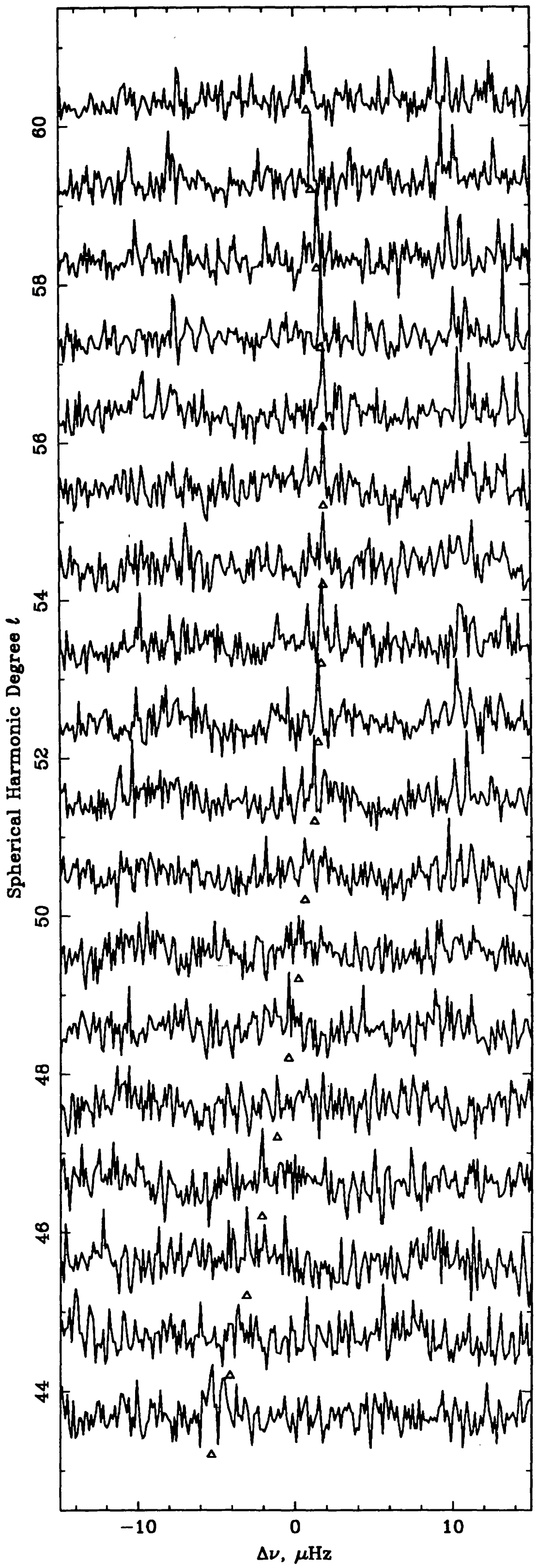

low frequency modes shown in this figure were not easily fitted by a Lorentzian, since the peaks were very sharp and signal-to-noise ratio was low. From those few multiplets the peaks were picked out by hand after plotting segments of the averaged power spectra on a graphics display terminal. This is not a very exact or even repeatable technique, but it was used in order to avoid holes in the l-ν diagram, and to push our mode identifications to the lowest possible frequencies.

Note that we were able to pick out mode peaks down to very low frequencies, as low as 1042 μHz for $l = 43$. Henning and Scherrer (1986) also claimed to see modes with $\nu_{nl} < 1.5$ mHz, but recently Gough and Kosovichev (1988) found that no plausible solar model is consistent with their frequencies. There is some considerable disagreement between the Henning and Scherrer (1986) frequencies and those of other researchers at low ν (frequency disagreements that are much greater than the mode line widths; see Duvall *et al.* 1988), which suggests that perhaps the Henning and Scherrer low-ν modes have been misidentified. A good check of this possibility would be to measure the velocity power per mode and compare with Libbrecht (1988*b*), since the power per mode is expected to show very little l-dependence below $l \sim 100$ (Libbrecht 1988*b*). An "echelle" plot using the current data set to show the low-ν modes is shown in Figure 3, which shows very clearly that we are observing real mode peaks. Measurements of these very low frequency modes show that the approximately power-law trend in the power per mode as a function of frequency at low frequencies presented by Libbrecht (1988*a*) continues down to $\nu = 1$ mHz.

Uncertainties, σ_{nl}, in the measured frequencies were determined two ways: (1) from the least-squares fits to Lorentzians, assuming the relative noise in the power spectra, σ_S/S, was constant over the frequency range of the fit, and (2) by fitting polynomial segments to ν_{nl} at fixed n, and measuring the scatter in the frequencies after subtracting the fit. For the latter technique, at each ν_{nl} a quadratic polynomial in l' was fitted to the frequencies with fixed n over the range $l - 4 \le l' \le l + 4$. After subtraction of the fit polynomial, the uncertainty, σ_{nl}, was estimated from the scatter in the residuals using standard error propagation and assuming normally distributed errors. Near the ridge endpoints, nine points were still used for the quadratic fit, but they were no longer centered on the mode of interest. Furthermore, σ_{nl} for the endpoint was arbitrarily taken to be 40% higher than that calculated from the scatter (a conservative step reflecting the fact that the last point on a ridge will normally have a higher uncertainty), and, for the next nearest point, σ_{nl} was increased by 20%. A comparison of the two error estimates showed that they gave essentially the same results. In Table 1 the 1 σ least-squares error estimates are quoted, except for the hand-picked modes, where the polynomial segment error estimate was used.

A comparison of frequencies with $l > 100$, shown in Figure 2, with those from Libbrecht and Kaufman (1988) reveals fre-

FIG. 3.—Sections of averaged power spectra from the low-l data set, plotted in an "echelle" plot, with the identified mode frequencies marked with triangles as in Fig. 1. The center frequency with $\Delta\nu = 0$ for each l segment corresponds to a frequency of $\nu = 1200 - 9(60 - l)$ μHz. At the higher l-values one can easily recognize the multiplet peaks, along with spatial sidelobes at a distance of $d\nu/dl \approx 9$ μHz from the main peak, and temporal sidelobes at distances of ± 11.6 μHz. For $l < 50$ the mode identifications are not so clear, since the signal-to-noise ratio is smaller. The $l = 45$ frequency, for example, was chosen by hand (see text) and was assigned to a lesser peak in order to fit the trend seen in this plot.

quency differences as large as 10 μHz between the two data sets. These large differences are almost certainly due to systematic errors in the older data, since the current data rely on sharply peaked Lorentzian fits, which are nearly free of systematic errors. Christensen-Dalsgaard, Gough, and Thompson (1988) have suggested the occurrence of such systematic errors in the Libbrecht and Kaufman (1988) data, based on a theoretical analysis of the frequencies. The Libbrecht and Kaufman (1988) data analysis used rather crude ridge fits, which are known to introduce some systematic errors, but the observed errors are much larger than expected, for which we have no obvious explanation; we suspect there may be some bug in the analysis software.

In order not to leave off the high-frequency modes, which cannot be separated into individual (nl) multiplets, we fitted the constant-n ridges at high ν to Gaussian functions of ν, correcting for systematic errors as described in equation (1). The resulting ridge fit mode frequencies are shown in Figure 2, along with the more accurate individual multiplet frequencies. Note how the ridge fits fill out the l-ν plane at high ν, although the determined frequencies are not without residual systematic errors. For the low-l data, it was found that a constant $s = 2.3$ and $\epsilon = 0$ in equation (1) gave an adequate agreement between the ridge fit frequencies and the mode frequencies determined from multiplet peaks. However, it was also apparent, using plots such as that shown in Figure 3 of Libbrecht and Kaufman (1988), that the ridge fit frequencies still contain systematic errors at the level of 1–2 μHz, even after making the above corrections. The source of the residual errors is not known, but it may be simply the limit of how accurately one can do with a simple Gaussian ridge fit at these low l. At the higher l, the systematic errors will be in general smaller, because $\partial\nu_{nl}/\partial l$ is smaller. The σ_{nl} for the ridge fits, presented in Table 1, were again determined from the scatter in the frequencies as a function of l, but multiplied by 1.4 to compensate for the fact the ridge fits are not completely independent of one another at adjacent l. The σ_{nl} in Table 1 do not include the systematic errors which we know are in these ridge fit data at the 1–2 μHz level.

For $4 \leq l \leq 140$ and low ν, the frequencies determined from the present BBSO data set have uncertainties that are much smaller than any previous measurements (see Duvall *et al.* 1988). However, for $l \leq 3$ the frequencies of Jiménez *et al.* (1987) are usually more accurate than those from the present data, and therefore for $l \leq 3$ the frequencies in Table 1 were obtained by merging the two data sets. Figure 4 is a key that shows which frequencies came from which source. Note that while the BBSO data set was obtained in 1986, near solar minimum, the Jiménez *et al.* (1987) frequencies are an average over 1977–1985. A comparison of the present 1986 BBSO data with similar 1988 data (Libbrecht and Woodard 1990) shows frequency differences that are strongly frequency-dependent, and are as high as a few tenths of a microhertz at high ν. This will introduce some slight systematic errors into the ν_{nl} in Table 1 for $l \leq 3$.

IV. THE INTERMEDIATE-RESOLUTION DATA SET

Full-disk intensity images of the Sun were obtained at BBSO on 1987 August 27 through an 8 Å passband filter centered on the Ca II K line. An image of the Sun of diameter approximately 1320 pixels was formed using the combination of a

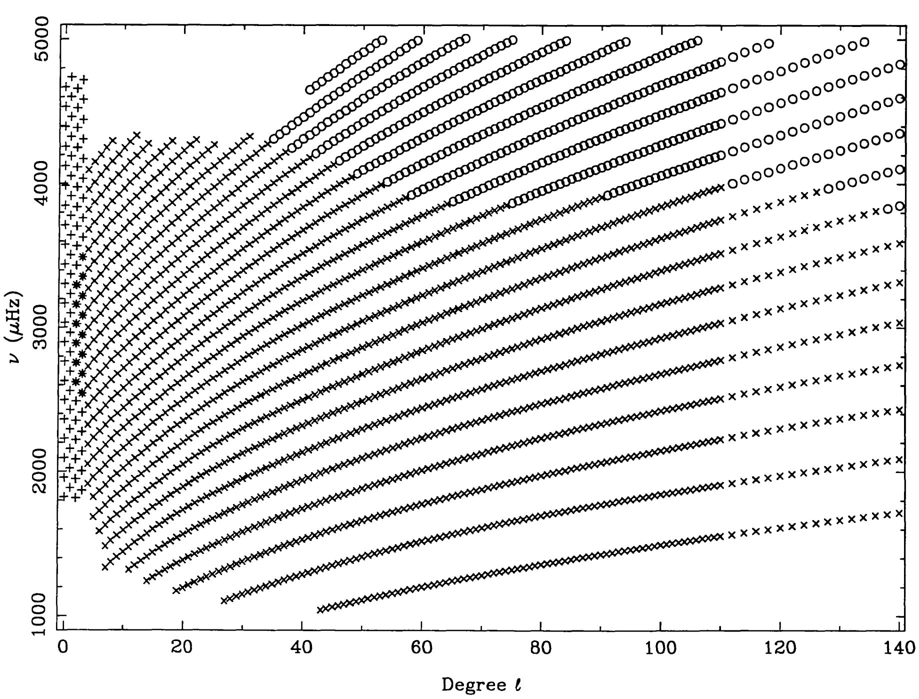

FIG. 4.—Schematic l-ν diagram showing the various sources of the low-l mode frequencies listed in Table 1. The plot includes (1) modes identified from Lorentzian fitting of multiplet peaks using the low-resolution data set (*crosses*); (2) very low l modes from Jiménez *et al.* (1987) (*plus signs*) (where there is an overlap in these two data sets [cross and plus sign both plotted], the frequencies were averaged to produce the entries in Table 1); and (3) frequencies determined from the Gaussian ridge fits of the BBSO data (*open circles*).

simple 12.5 cm diameter objective lens and a small diverging lens. The optics and camera were fastened to an optical bench mounted on the side of the 20 cm Singer-Link telescope which was guided by the main 65 cm refractor at BBSO. A Datacopy Model 610 Electronic Digitizing Camera, a scanning CCD camera, was used to produce byte-deep images in a 1408 pixel by 1408 scan line format once every 90 s. The time required to complete a 1408 line scan is 46.5 s.

From a time series of 346 images, spanning a period of 9.5 hr, the power in the Ca II K brightness fluctuations was computed as a function of l, m, and ν by the procedure outlined in § II. The bulk of these calculations was performed on a CONVEX C1-XP computer belonging to the Caltech Astronomy Department. To keep computation time to a reasonable level, spectra were computed only for $2 \leq l \leq 400$ and even m in the range $2 \leq |m| \leq l$ for each l. Power was, in fact, seen in preliminary spectra of these data up to $l \approx 900$. A preliminary l-ν diagram of the resulting averaged power spectra was presented by Woodard and Libbrecht (1988), who noted that the nonnegligible scan time of the instrument affects the measurement of frequency splittings due to solar rotation. However, scanning is not expected to affect the mode frequencies averaged over m.

An initial selection of modes was made by examining 150 μHz intervals in the power spectra corresponding to each mode in a table of mode frequencies interpolated from the table of Libbrecht and Kaufman (1988). The criterion for the acceptance of a mode, though somewhat subjective, was basically the presence, within the mentioned frequency interval, of a single, unambiguous peak produced by the unresolved mode of interest and its unresolved spatial sidelobes. Acceptable frequency intervals were then fitted to the sum of a Gaussian and a constant function as described in § II. Modes for which adequate fits could not be obtained were then rejected. For each measured frequency ν_{nl}, a quadratic function of l' was fitted to all available frequencies $\nu_{nl'}$ for which $l - 15 \leq l' \leq l + 15$. The random error in ν_{nl} was estimated from the scatter about the fit. In this way a table of approximate mode frequencies and power was obtained.

The dominant source of systematic error is expected to be the variation of mode power with frequency at fixed l, as described by the $\partial P(\nu, l)/\partial\nu$ term in equation (1) [the $\partial P(\nu, l)/\partial l$ term being negligible here]. As noted elsewhere (Libbrecht *et al.* 1986), the dependence of mode power on ν and l is approximately separable as a function of ν times a function of l. Exploiting this fact, the frequency dependence of mode power was first estimated by dividing an interval in frequency into equal bins and averaging the measured power of all modes within each bin. The natural log of the average power versus bin frequency was then fitted to a quadratic function of frequency and the quantity $\partial \log P/\partial\nu$ determined from the fit. Both a lower frequency interval, 2200–3150 μHz, and an upper interval, 3150–4555 μHz, were treated separately, since $\partial \log P/\partial\nu$ changes both sign and magnitude rather abruptly at ~ 3150 μHz in the binned data. The number of bins was 50 for both ranges. The relevant correction term in equation (1), then applied to the mode frequencies, used the fit value of $\partial \log P/\partial\nu$ for the appropriate frequency range. For a given n, the quantity $d\nu/dl$ needed for this correction was derived from an unweighted fit of all the measured ν_{nl}^2 to a cubic polynomial in l. The overlap parameter, s, also needed here, cannot be straightforwardly estimated from the present Ca II K brightness data because the frequency widths of the ridges reflect mainly the short duration of the data and not the l resolution. Instead we estimated s from the p-mode oscillation spectrum obtained from a set of Ca II K brightness images taken at the South Pole (Duvall *et al.* 1988). The South Pole data are similar to ours, though of considerably lower spatial resolution. They are of sufficiently long duration to resolve spatial sidelobe structure. A value of $s \approx 2$ was obtained by fitting a Gaussian to the average spectrum presented in Figure 4b of Duvall *et al.* (1988). The corrected intermediate-l frequencies were then compared with the low-l frequencies described in § III for $30 \leq l \leq 140$. Only low-l modes obtained by peak fitting were used in this comparison. Figure 5 is an l-ν plot showing the intermediate-l frequencies together with the comparison low-l frequencies. By plotting frequency differences of these two sets against the various correction terms appearing in equation (1), systematic discrepancies up to ~ 1 μHz were revealed, which would have essentially been removed had the value $s = 3$ been used in the correction formula instead. Since this large an s cannot be observationally justified, we conclude that some unknown source of systematic error is likely present at the sub-μHz level. Some of the discrepancy between the two data sets may be caused by temporal changes in mode frequencies. Based on these comparisons, a possible correction to the image scale was deemed unnecessary. We note that failure to take into account the nonzero angular semidiameter of the Sun, when projecting these images onto a standard orientation, roughly mimics a scale error and can result in substantial frequency errors. Therefore, the transformation of the raw images described by Libbrecht and Zirin (1986) has been appropriately modified for the intensity data. Although spurious ridges, due to temporal Nyquist aliasing, are present in our intermediate-resolution l-ν spectrum, there is little reason to believe that they lead to significant frequency errors. For example, there are no obvious irregularities in Figure 5 to mark the crossings of aliased and true power ridges.

The final set of frequencies for the intermediate-resolution data set is given in Table 1 for every n and every fifth l. The frequency entry for each n and l is the average of the individual $\nu_{nl'}$ for $l - 2 \leq l' \leq l + 2$. We note that the frequencies of modes obtained with the present intermediate-resolution data differ from the corresponding mode frequencies obtained by Libbrecht and Kaufman (1988) by as much as ~ 12 μHz, confirming the systematic errors in the latter data set mentioned above.

V. THE HIGH-RESOLUTION DATA SET

The high-resolution observations were taken on 1987 July 23 from 15:00 to 01:00 UT. This was a day of moderate-quality seeing. The data were collected on the BBSO 25 cm refractor using the videomagnetograph system configured for Doppler measurements (Zirin 1985). This system operates in much the same fashion as that on the dedicated helioseismology telescope described in § III. As with the low-resolution data, the 6439 Å Ca line was used. The data consist of 633 Doppler images, taken at a rate of one per minute, consisting of 498 × 460 pixels, with an image size of approximately

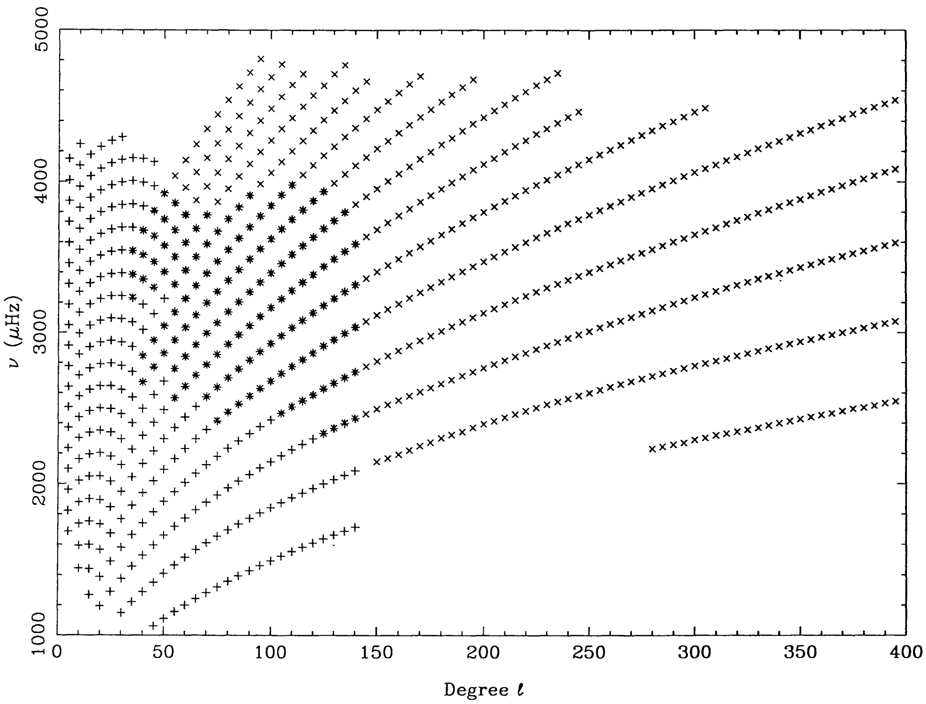

FIG. 5.—Schematic l-ν diagram showing the intermediate-l frequency determinations (*crosses*) along with the low-l frequencies (*plus signs*).

$267'' \times 197''$ centered on the solar disk. This data set was originally made for the purpose of measuring velocity power as a function of l at high l (Kaufman 1988). Such measurements are easily affected by atmospheric seeing. To correct for this effect, the telescope was moved from the center disk to the limb, at approximately 15 minute intervals, and a series of short-exposure limb profiles were acquired. This was accomplished without interrupting the collection of Doppler images. Atmospheric seeing was then quantitatively determined from smearing of the limb profile. In this work, unlike that of Kaufman (1988), no correction for the effects of seeing has been made. After interpolating over bad or missing images, and subtracting a best-fit planar background from each image, a two dimensional spatial Fourier transform was performed on each image, giving a k_x-k_y-t diagram. This is equivalent to making a plane-wave approximation to the spherical harmonics. For each time series of spatial frequency components, a best-fit linear background was subtracted. Temporal Fourier transforms were then done, resulting in a k_x-k_y-ω diagram. We then corrected for frequency shifts produced by solar rotation, and integrated the data along circles of constant $k_h = (k_x^2 + k_y^2)^{1/2} = [l(l+1)]^{1/2}/R_\odot$, thereby producing averaged power spectra, $S_k(\nu)$, where k is an integer index corresponding to the spectral components in the spatial Fourier transform. This procedure is analogous to the full-disk analysis procedure of azimuthally averaging the rotationally corrected $S_{lm}(\nu)$ spectra to get averaged power spectra, $S_l(\nu)$. See Hill (1988) for further explanation of this procedure. Collectively, the $S_k(\nu)$ form a k_h-ω (or l-ν) diagram, and, as seen in Figure 6, ridges can be seen out to $l \sim 1800$.

Since individual modes cannot be identified in these data, mode frequencies were estimated by fitting the power spectra, $S_k(\nu)$, to a series of Gaussians,

$$S_k(\nu) \to \sum_{i=1}^{N} A_i \exp\left[-(\nu - \nu_i)^2/\sigma_i^2\right] + A_B \exp\left[-(\nu - \nu_B)^2/\sigma_B^2\right] + C, \quad (4)$$

where ν_i is the frequency of the ith ridge, the subscript B refers to a wide background Gaussian, and C is a constant background offset. A first attempt at fitting the above equation to $S_k(\nu)$ gave adequate results except where the frequency of the background Gaussian came to within ≈ 300 μHz of equaling the frequency of the f ridge. This occurred for $l \gtrsim 1100$, and for these spectra the f-mode frequency and width were sufficiently close to the background frequency and width to prevent the fitting algorithm from converging on appropriate values for the f-mode and background amplitudes. Below $l \approx 1100$ the fitting algorithm was well behaved, and we determined that both ν_B and σ_B varied approximately linearly with l. This fact was exploited by redoing the fits to equation (4) with ν_B and σ_B no longer free parameters. We used $\nu_B = 3126 + 8.55k$ μHz and $\sigma_B = 648 + 5.58k$ μHz. This allowed the fitting algorithm to converge to sensible values A_f and A_B. Typical power spectra and their fits are shown in Figure 7. Typically, the σ_i were found to be about 60–200 μHz, and are certainly not indicative of the intrinsic mode line widths, at least in the regimes previously explored by the low- and intermediate-resolution data sets. Note that in the $k = 80$ ($l \approx 1683$) spectrum, the Gaussian component of the background noise is clearly visible,

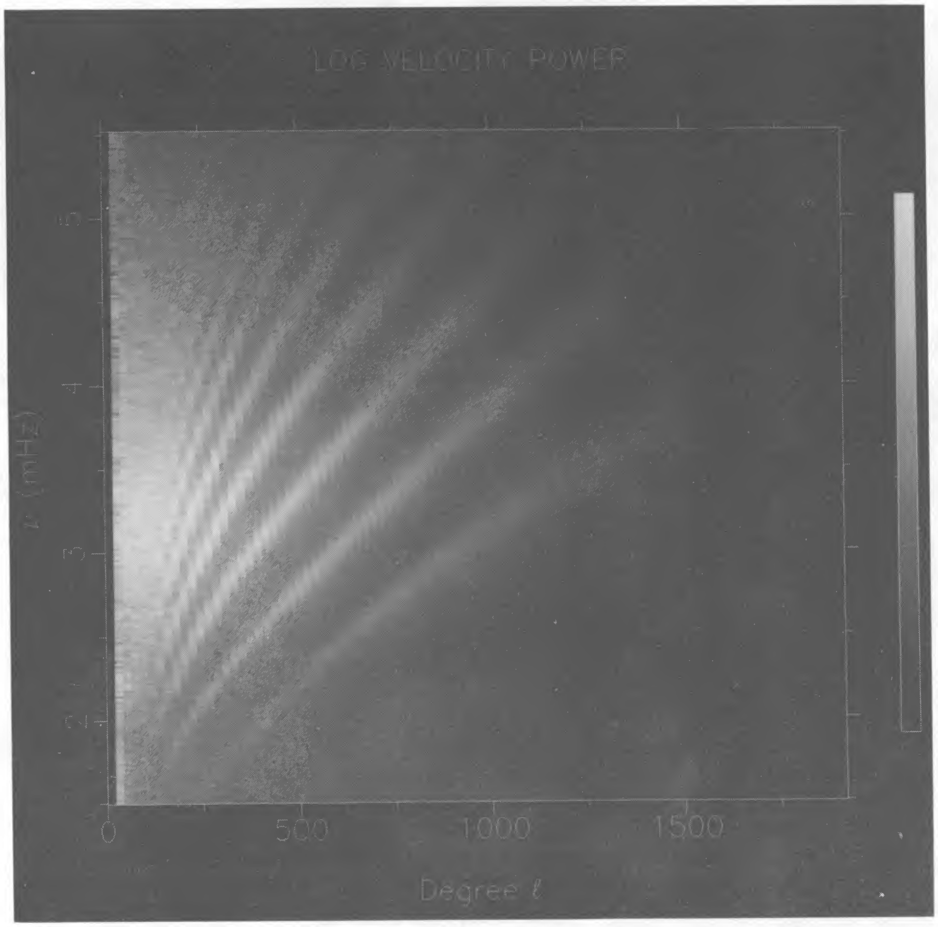

FIG. 6.—An l-ν power diagram showing the high-resolution data. Power can be seen out to $l \approx 1800$. For this diagram we have used a scale factor of $dl/dk = 21.344$.

and appears as a shoulder on the low-frequency side of the $n = 0$ ridge. For $l \lesssim 1500$, A_B is a constant 20% of the maximum ridge amplitude at fixed l, $A_{i,max}(l)$, and by $l \approx 1880$ it increases to a factor of 3 greater than $A_{i,max}(l)$. Similarly, for the velocity power P (which is proportional to $\sigma_j A_j$), $P_B(l)/P_{i,\max}(l) \approx 1$ until $l \approx 1500$, and then increases with l to ~ 20 at $l \approx 1880$.

The cause of this background noise is known. There are two major classes of possible explanations. One is that the background noise is a real solar phenomenon. Duvall and Harvey (1986) have suggested a possible mechanism whereby large-scale convective turbulence (such as supergranulation) modulates the spatial frequency of the oscillations, thereby producing a plethora of nearby sidebands. If the sidebands are closely spaced and if the spatial frequency resolution is relatively poor, the sidebands could appear as background noise in the 5 minute band. Duvall and Harvey (1986) even suggest that this effect has been seen in their data at $l = 150m$ however, only at the 2% level. The other class of explanations is that the noise is due to some sort of spurious Doppler signal introduced into the data. Heterodyning of low temporal frequency, large-velocity signals (again, such as supergranulation) by seeing can introduce broad-band noise (Ulrich *et al.* 1984). Phase jitter could also have been introduced by imperfect repointing of the telescope after the above-described seeing measurements. Changes in the angle of arrival of a light beam entering a birefringent filter produce changes in the spectral response of the filter. If the filter used in these observations was not perfectly telecentrically located in the optical path, then angle-of-arrival changes produced by seeing would cause spectral response changes which would amplitude-modulate the Doppler oscillation signal (Grigoryev and Kobanov 1988). Again, this could produce sidebands which would show up as a background noise at 5 minutes.

The l-ν diagram was calibrated by comparing the ridge frequencies in the range $150 \leq l \leq 400$ with those determined from the intermediate-resolution data set. Using this method, we found a scale factor, dl/dk, which agreed adequately with a less accurate scale factor determined directly from the images.

The main systematic errors in the frequency determinations are described by equation (1). As with the intermediate-resolution data, the parameter s cannot be straightforwardly estimated from the data because of the artificially large ridge widths. Instead, we considered the plane-wave approximation to the spherical harmonic overlap function, $V(l, l')$, finding $V(l, l') \approx \mathrm{sinc}^2[\pi \Delta l/(dl/dk)]$. The small scale error, α, is not

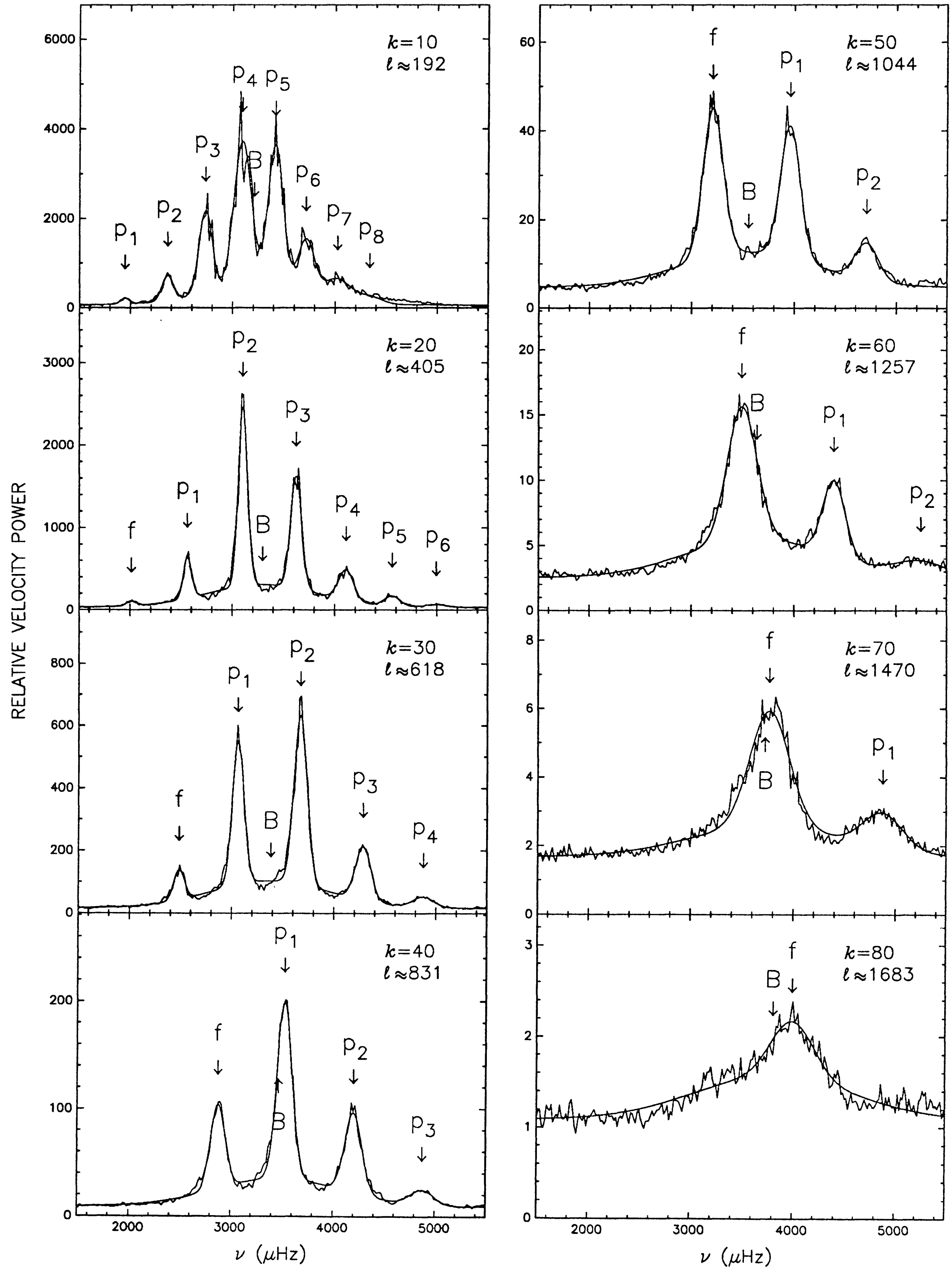

FIG. 7.—Typical power spectra from the high resolution data (shown in Fig. 6) and their Gaussian ridge fits (i.e., fits to eq. [4] in the text). Also shown are the ridge identifications (f and p_i, along with the Gaussian component of the background noise (B).

included here and is dealt with elsewhere. The formalism developed in equation (1) can still be used if we approximate the plane-wave mode leakage function by a Gaussian of the appropriate width. By matching the FWHM of the sinc^2 function with that of a Gaussian, we obtained $s = 0.3762 dl/dk \approx 8$. This produces corrections that range from -4 to $+9$ μHz. The corrected frequencies were then used to recalibrate the l-ν diagram using the above method, giving a new scale factor of $dl/dk = 21.344 \pm 0.013$. Figure 8 shows the region of overlap between the intermediate-l frequencies and the corrected high-l frequencies.

The corrected frequencies were interpolated using a cubic spline onto a grid with integral l and spacing of 20. Random errors in the frequencies, σ_{nl}, were determined by polynomial fits to the ridge frequencies as described in § II. Typically a 25 point (corresponding to a range in l of 480) fit was used, except when there were less than 25 points in the ridge. In these cases, the quadratic was fitted to the largest odd number of points in the ridge. At the ends of a ridge, 25 points (if available) were still used in the fit, but they were no longer centered on the mode of interest. As in § IV, by plotting the frequency differences between high- and intermediate-l data sets against

$$\frac{1}{2} s^2 \frac{d\nu}{dl} \frac{1}{P} \frac{\partial P(n, l)}{\partial l}$$

and $\epsilon l(d\nu/dl)$ from equation (1), we find that the residual systematic errors are of the order of ± 20 μHz, with considerable scatter. However, the random errors in the high-l frequencies are considerably greater than those in the intermediate-l frequencies. When this is taken into account, we find that the systematic errors in the high-l frequencies are probably no greater than the associated random errors. We, therefore, conservatively estimated that the remaining systematic errors are equal to the random errors. The final frequency uncertainty for a single mode can be found by adding, in quadrature, the random and systematic errors. This amounts to multiplying the random error by $\sqrt{2}$. Table 1 contains the high-l frequencies and their uncertainties for $l > 400$. For $l \leq 400$, in the case where the high-resolution data set covers a region of the l-ν plane not previously covered by the intermediate-resolution data set, the high-l frequencies are also presented. Figure 8 can be used as a guide for finding which $l \leq 400$ frequencies come from the high-resolution data set. The σ_{nl} in Table 1 do not include the assumed remaining systematic errors. All of the high-l frequencies and their uncertainties are plotted schematically in Figure 9. Also plotted in Figure 9 is the simplest theoretical expression for the f-mode, $\omega^2 = gk$, or, equivalently, $\nu = 3158(l/1000)^{1/2}$ μHz.

As can be seen from Figure 9, there is a considerable discrepancy between the observed and the theoretical values of the f-mode frequencies, going to as much as 150 μHz at $l = 1860$. We are unable to explain this discrepancy. It could be real, in which case it might be caused by the presence of an exponentially decaying, horizontal chromospheric magnetic field, or perhaps an unusual density structure in the solar atmosphere. Roberts and Campbell (1988) and Campbell and Roberts (1989) have analyzed such a case, but they predict that the f-mode frequencies would *increase* by as much as 127 μHz at $l = 1300$ for a 200 G field. Evans and Roberts (1990) have examined the case of a uniform chromospheric magnetic field and found even greater f-mode frequency shifts. However,

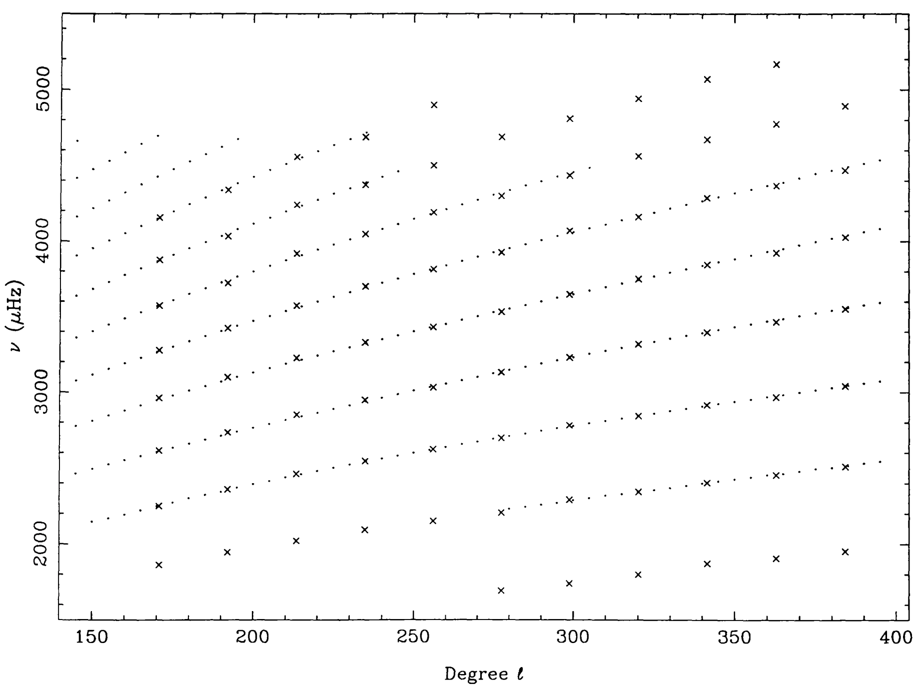

FIG. 8.—Schematic l-ν diagram showing the overlap region of the intermediate-l frequencies (*dots*) and the high-l ridge fit Gaussian centroids, corrected for systematic effects described by eq. (1) (*crosses*). Note that certain regions of the l-ν plane for $l \leq 400$ are covered only by the high-resolution data set frequencies.

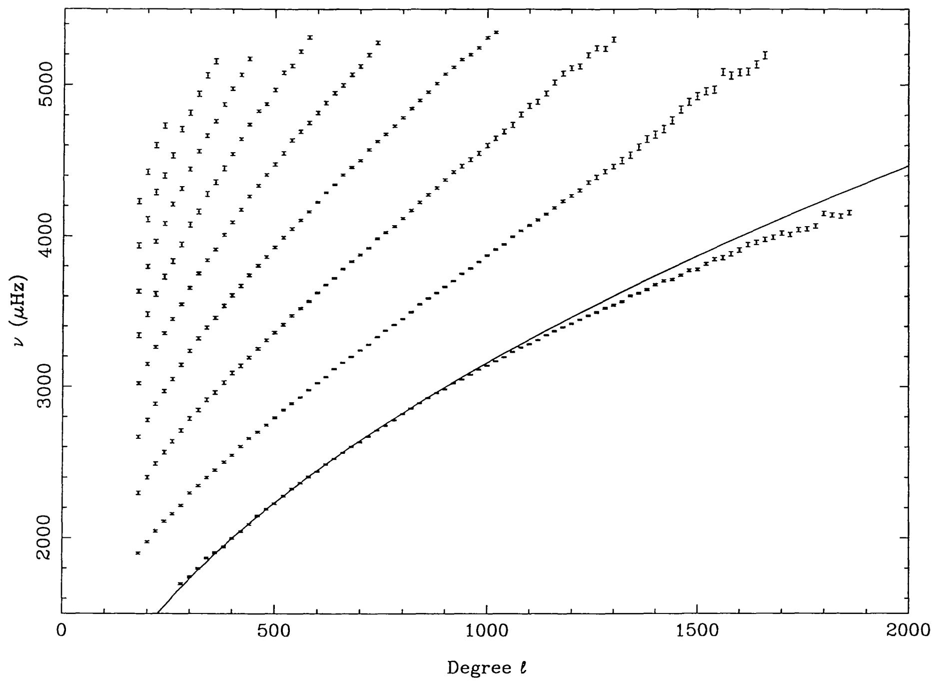

FIG. 9.—Schematic l-ν diagram showing the high-l frequency determinations and their uncertainties. All of these frequencies for $l > 400$ and a few for $l \leq 400$ appear in Table 1. Also plotted is the theoretical expectation for the f-mode ridge, $\omega^2 = gk$. Note that at high l the measured f-mode frequencies are significantly below the theoretical expectation.

these are, again, frequency increases. We cannot exclude the possibility that the frequency discrepancy could also be due to unknown systematic effects, such as differential image motion, and misregistration between images induced by seeing and telescope shake. Hill (1984) has modeled the effects of differential image motion on modes with l ranging from 500 to 550 and found that frequency differences up to 12 μHz can be produced. However, the difference is not systematically high or low, and the simulation assumes that the seeing is much worse than what would normally be encountered at any ground-based observatory. Finally, the f-mode frequencies might be pulled downward by the presence of the background noise.

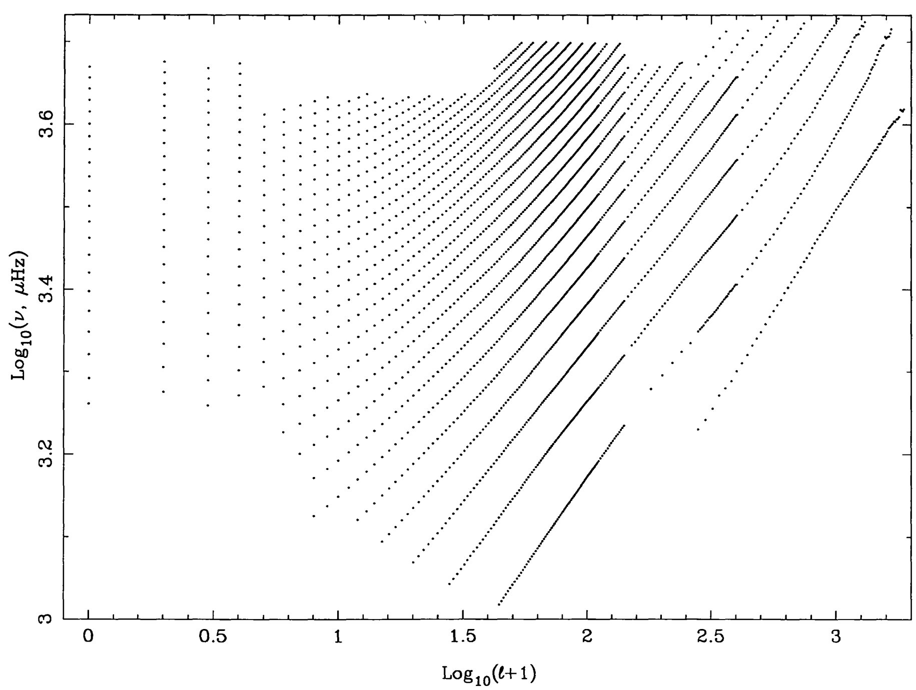

FIG. 10.—A log-log l-ν diagram showing all the frequencies in Table 1

The background noise appears as a straight ridge in the l-ν plane which crosses below the f ridge at $l \approx 1400$ and as noted above, makes the f ridge look asymmetric. This asymmetry could cause the centroid of the Gaussian fit to be shifted toward lower frequencies. However, we believe that we have accounted for this effect by including the appropriate background terms in equation (4). Also, the frequency discrepancy starts to appear at $l \approx 1000$, which is well before the background ridge crosses below the f ridge. If this pulling effect were the cause of the frequency differences, we would expect that the observed frequencies would be greater than the theoretical values for $l \lesssim 1000$, which is not observed.

VI. SUMMARY

In summary, we have observed solar oscillations at three different spatial scales at Big Bear Solar Observatory during 1986–1987, and using the three data sets, we have compiled a new and more accurate table of solar oscillation frequencies. The identified oscillation modes are presented in Table 1, and are also shown in Figure 10. We can identify several areas of future work which would improve the table still further: (1) a more accurate modeling of the ridges should produce more accurate frequency determinations than the Gaussian ridge fits, and may reduce the residual systematic errors; (2) with better data it would be desirable to observe coherent f-modes at low l; (3) further observations are needed at high spatial resolution to determine more accurately the f-mode frequencies at high l, to confirm the rather large deviation from theoretically expected frequencies that we have measured. The frequency data in Table 1 may be obtained in digital form from the authors at the address below.

We wish to thank the observing staff at BBSO for their assistance in obtaining the three data sets analyzed here. Some of the computations were performed at the San Diego Supercomputer Center, and the work was supported in part by National Science Foundation contracts ATM-8604632 and AST-8657393. J. M. K. was supported in part by NASA Training Grant NGT-50187.

REFERENCES

Campbell, W. R., and Roberts, B. 1989, *Ap. J.*, **338**, 538.
Christensen-Dalsgaard, J. 1988, in *Seismology of the Sun and Sun-like Stars*, ed. E. J. Rolfe (Noordwijk: ESA), p. 431.
Christensen-Dalsgaard, J., Duvall, T. L., Gough, D. O., Harvey, J. W., and Rhodes, E. J. 1985, *Nature*, **315**, 378.
Christensen-Dalsgaard, J., Gough, D. O., and Thompson, M. J. 1988, in *Seismology of the Sun and Sun-like Stars*, ed. E. J. Rolfe (Noordwijk: EAS), p. 493.
Christensen-Dalsgaard, J., Gough, D. O., and Toomre, J. 1985, *Science*, **229**, 923.
Deubner, F.-L., and Gough, D. 1984, *Ann. Rev. Astr. Ap.*, **22**, 593.
Duvall, T. L., Jr., and Harvey, J. W. 1986, in *Seismology of the Sun and Distant Stars*, ed. D. O. Gough (Dordrecht: Reidel), p. 105.
Duvall, T. L., Harvey, J. W., Libbrecht, K. G., Popp, B. D., and Pomerantz, M. A. 1988, *Ap. J.*, **324**, 1158.
Elsworth, Y., Isaak, G. R., Jefferies, S. M., McLeod, C. P., New, R., Pallé, P. L., Régulo, C., and Roca Cortés, T. 1988, in *Seismology of the Sun and Sun-like Stars*, ed. E. J. Rolfe (Noordwijk: ESA), p. 27.
Evans, D. J., and Roberts, B. 1990, *Ap. J.*, **356**, 704.
Gough, D. O., and Kosovichev, A. G. 1988, in *Seismology of the Sun and Sun-like Stars*, ed. E. J. Rolfe (Noordwijk: ESA), p. 195.
Grigoryev, V. M., and Kobanov, N. I. 1988, *Astr. Ap.*, **197**, 345.
Henning, H. M., and Scherrer, P. H. 1986, in *Seismology of the Sun and Distant Stars*, ed. D. O. Gough (Dordrecht: Reidel), p. 55.
Hill, F. 1984, in *Solar Seismology from Space*, ed. R. K. Ulrich (Pasadena: JPL), p. 255.
———. 1988, *Ap. J.*, **333**, 996.
Hogbom, J. A. 1974, *Astr. Ap. Suppl.*, **15**, 417.
Jimeñez, A., Pallé, P. L., Peŕez, J. C., Régulo, C., Roca Cortés, T., Isaak, G. R., McLeod, C. P., and van der Raay, H. B. 1987, in *IAU Symposium 123, Advances in Helio- and Asteroseismology*, ed. J. Christensen-Dalsgaard and S. Frandsen (Dordrecht: Reidel), p. 205.
Kaufman, J. M. 1988, in *Seismology of the Sun and Sun-like Stars*, ed. E. J. Rolfe (Noordwijk: ESA), p. 31.
Libbrecht, K. G. 1988*a*, *Space Sci. Rev.*, **47**, 275.
———. 1988*b*, *Ap. J.*, **334**, 510.
———. 1989, *Ap. J.*, **336**, 1092.
Libbrecht, K. G., and Kaufman, J. M. 1988, *Ap. J.*, **324**, 1172.
Libbrecht, K. G., Popp, B. D., Kaufman, J. M., and Penn, M. J. 1986, *Nature*, **323**, 235.
Libbrecht, K. G., and Woodard, M. F. 1990, *Nature*, **345**, 779.
Libbrecht, K. G., and Zirin, H. 1986, *Ap. J.*, **308**, 413.
Roberts, B., and Campbell, W. R. 1988, in *Seismology of the Sun and Sun-like Stars*, ed. E. J. Rolfe (Noordwijk: ESA), p. 311.
Ulrich, R. K., Rhodes, E. J., Jr., Cacciani, A., and Tomczyck, S. 1984, in *Solar Seismology from Space*, ed. R. K. Ulrich (Pasadena: JPL), p. 263.
Vorontsov, S. V., and Zharkov, V. N. 1989, *Soviet Sci. Rev. E, Ap. Space Phys.*, **7**, 1.
Woodard, M. F., and Libbrecht, K. G. 1988, in *Seismology of the Sun and Sun-like Stars*, ed. E. J. Rolfe (Noordwijk: ESA), p. 67.
Zirin, H. 1985, *Australian J. Phys.*, **38**, 961.

K. G. LIBBRECHT, M. F. WOODARD, and J. M. KAUFMAN: California Institute of Technology, Solar Astronomy 264-33, 1201 East California Boulevard, Pasadena, CA 91125
[INTERNET: xxx@sundog.caltech.edu, where xxx=kgl, mfw, jim]

(Table 1 follows)

TABLE 1

SOLAR OSCILLATION FREQUENCIES[a]

$n \backslash l$	0	1	2	3	4	5	6	7	8	9
6	-	-	-	-	-	-	-	1334.60±0.04	1372.12±0.04	1408.47±0.03
7	-	-	-	-	-	-	-	1483.50±0.05	1521.25±0.04	1557.61±0.02
8	-	-	-	-	-	-	1587.48±0.05	1627.59±0.03	1665.77±0.04	1702.46±0.04
9	-	-	-	-	-	1685.84±0.03	1727.77±0.05	1767.69±0.02	1806.20±0.03	1843.61±0.04
10	-	-	-	-	-	1823.33±0.16	1866.15±0.07	1906.86±0.03	1946.11±0.03	1984.25±0.04
11	-	-	1815.40±0.10	1868.20±1.20	1914.68±0.11	1960.56±0.05	2003.99±0.08	2045.92±0.04	2086.18±0.03	2125.20±0.04
12	1823.60±0.60	1885.50±0.40	1947.50±0.40	2003.40±0.60	2051.80±0.17	2098.45±0.06	2142.51±0.04	2184.58±0.04	2225.23±0.05	2264.68±0.05
13	1957.30±0.40	2020.70±0.40	2084.10±0.30	2138.70±0.30	2188.30±0.17	2235.47±0.06	2279.86±0.06	2322.19±0.06	2362.90±0.05	2402.40±0.05
14	2093.50±0.20	2156.70±0.40	2218.40±0.30	2274.70±0.30	2324.14±0.13	2371.21±0.05	2415.55±0.07	2458.16±0.06	2499.43±0.06	2539.53±0.05
15	2228.60±0.10	2291.90±0.20	2352.20±0.20	2409.40±0.30	2458.46±0.10	2506.11±0.08	2551.17±0.06	2594.27±0.07	2636.11±0.07	2677.02±0.05
16	2362.50±0.10	2426.10±0.20	2486.80±0.10	2541.50±0.21	2593.00±0.10	2641.07±0.07	2687.14±0.07	2731.16±0.08	2773.74±0.05	2815.24±0.06
17	2496.60±0.30	2558.90±0.20	2619.82±0.23	2676.83±0.22	2728.44±0.07	2777.32±0.08	2823.69±0.07	2868.26±0.09	2911.59±0.05	2953.57±0.06
18	2629.60±0.30	2693.60±0.30	2754.67±0.17	2811.29±0.17	2864.17±0.07	2913.54±0.09	2960.69±0.06	3005.66±0.06	3049.10±0.06	3091.44±0.07
19	2764.40±0.10	2828.10±0.20	2889.96±0.16	2947.33±0.20	3000.17±0.07	3049.85±0.06	3097.28±0.09	3142.79±0.09	3186.61±0.06	3229.45±0.06
20	2899.30±0.10	2963.30±0.20	3024.30±0.09	3082.63±0.21	3135.86±0.08	3186.12±0.07	3234.04±0.07	3279.76±0.10	3324.28±0.07	3367.75±0.08
21	3033.80±0.10	3098.70±0.10	3159.78±0.20	3217.94±0.20	3271.39±0.11	3322.48±0.09	3370.99±0.10	3417.38±0.12	3462.49±0.10	3506.03±0.08
22	3168.60±0.20	3233.20±0.30	3295.68±0.25	3354.28±0.18	3408.04±0.12	3459.57±0.10	3508.06±0.09	3555.31±0.11	3600.85±0.11	3644.77±0.11
23	3304.10±0.30	3368.90±0.10	3431.20±0.20	3489.36±0.35	3544.25±0.21	3597.00±0.11	3646.02±0.14	3692.97±0.23	3739.28±0.19	3784.04±0.19
24	3439.80±0.30	3504.60±0.20	3567.20±0.50	3626.10±0.30	3681.74±0.20	3734.52±0.19	3784.07±0.26	3831.48±0.23	3877.82±0.25	3923.62±0.30
25	3576.30±0.60	3640.20±0.40	3703.30±0.20	3760.90±0.30	3818.88±0.47	3871.96±0.51	3922.17±0.36	3969.71±0.29	4016.17±0.34	4062.07±0.35
26	3711.50±0.20	3777.40±0.70	3837.80±0.80	3897.60±0.60	3958.16±1.55	4009.61±0.49	4060.94±0.42	4108.37±0.40	4155.07±0.44	4201.87±0.56
27	3847.40±1.00	3914.10±0.70	3975.50±0.40	4035.00±0.70	4095.27±1.35	4150.85±1.21	4201.13±0.69	4249.24±0.49	4295.91±0.69	-
28	3984.90±0.30	4052.10±0.70	4112.90±0.40	4171.70±0.70	-	-	-	-	-	-
29	4121.90±0.40	4189.80±0.40	4249.30±0.50	4308.60±1.00	-	-	-	-	-	-
30	4257.40±0.40	4325.60±0.30	4387.30±0.40	4443.80±0.80	-	-	-	-	-	-
31	4394.90±0.20	4463.60±0.70	4524.20±0.40	4583.50±0.30	-	-	-	-	-	-
32	4532.30±0.80	4600.80±0.20	4656.90±0.80	4717.40±0.60	-	-	-	-	-	-
33	4668.60±0.50	4738.60±0.70	-	-	-	-	-	-	-	-

[a] In units of 10^{-6} Hz; l = spherical harmonic degree, n = radial order.

$n \backslash l$	10	11	12	13	14	15	16	17	18	19
3	-	-	-	-	-	-	-	-	-	1173.25±0.03
4	-	-	-	-	1242.54±0.03	1268.60±0.02	1293.72±0.02	1318.05±0.03	1341.54±0.02	1364.30±0.02
5	-	1320.47±0.04	1351.91±0.03	1382.34±0.01	1411.73±0.02	1440.06±0.01	1467.29±0.02	1493.48±0.02	1518.76±0.01	1543.06±0.01
6	1443.40±0.03	1477.19±0.02	1509.71±0.02	1541.14±0.01	1571.58±0.02	1601.04±0.01	1629.50±0.01	1657.05±0.01	1683.65±0.02	1709.38±0.02
7	1592.91±0.02	1627.11±0.02	1660.28±0.02	1692.41±0.02	1723.56±0.01	1753.81±0.02	1783.25±0.02	1812.00±0.02	1840.04±0.02	1867.34±0.02
8	1737.84±0.02	1772.23±0.03	1805.78±0.02	1838.73±0.02	1870.86±0.02	1902.37±0.03	1933.11±0.03	1963.35±0.04	1992.84±0.04	2021.80±0.02
9	1879.98±0.02	1915.41±0.03	1950.00±0.03	1983.79±0.04	2017.03±0.04	2049.69±0.03	2081.62±0.04	2113.06±0.04	2143.77±0.03	2173.79±0.04
10	2021.53±0.06	2058.00±0.04	2093.65±0.04	2128.52±0.05	2162.54±0.04	2195.85±0.04	2228.44±0.05	2260.36±0.05	2291.66±0.04	2322.30±0.04
11	2162.99±0.04	2199.84±0.05	2235.94±0.04	2271.16±0.04	2305.73±0.04	2339.48±0.04	2372.61±0.05	2404.96±0.04	2436.77±0.04	2468.23±0.04
12	2302.80±0.05	2340.09±0.05	2376.37±0.04	2411.85±0.05	2446.75±0.04	2481.06±0.04	2514.79±0.04	2548.15±0.04	2580.81±0.04	2613.07±0.04
13	2440.75±0.05	2478.55±0.05	2515.44±0.05	2551.71±0.04	2587.26±0.04	2622.31±0.04	2656.92±0.04	2691.03±0.04	2724.66±0.03	2757.94±0.04
14	2578.64±0.04	2616.98±0.05	2654.59±0.05	2691.69±0.05	2728.21±0.07	2764.09±0.03	2799.47±0.04	2834.34±0.03	2868.65±0.04	2902.45±0.04
15	2716.95±0.05	2756.13±0.05	2794.50±0.04	2832.15±0.06	2869.17±0.04	2905.75±0.04	2941.72±0.05	2977.19±0.03	3012.16±0.03	3046.48±0.04
16	2855.70±0.05	2895.33±0.05	2934.31±0.05	2972.56±0.05	3010.07±0.05	3047.05±0.04	3083.40±0.04	3119.41±0.04	3154.81±0.03	3189.70±0.04
17	2994.44±0.06	3034.53±0.05	3073.76±0.04	3112.47±0.05	3150.57±0.04	3188.00±0.05	3224.95±0.04	3261.37±0.04	3297.29±0.04	3332.94±0.05
18	3132.88±0.05	3173.39±0.04	3213.23±0.05	3252.27±0.05	3290.83±0.05	3328.74±0.04	3366.28±0.05	3403.41±0.06	3439.94±0.05	3475.89±0.06
19	3271.18±0.07	3312.38±0.07	3352.74±0.05	3392.35±0.06	3431.35±0.07	3470.13±0.07	3507.79±0.05	3545.49±0.07	3582.60±0.06	3619.35±0.06
20	3410.10±0.08	3451.72±0.07	3492.27±0.07	3532.47±0.07	3571.97±0.08	3611.18±0.07	3649.90±0.09	3687.88±0.08	3725.60±0.09	3762.60±0.12
21	3549.07±0.09	3591.19±0.08	3632.38±0.09	3673.24±0.09	3713.35±0.13	3752.74±0.17	3791.50±0.15	3829.95±0.13	3868.12±0.20	3906.40±0.15
22	3688.24±0.13	3730.74±0.13	3772.75±0.14	3813.78±0.20	3854.35±0.18	3893.79±0.18	3933.82±0.28	3971.68±0.31	4010.90±0.33	4048.98±0.29
23	3827.34±0.21	3870.58±0.22	3912.59±0.20	3955.33±0.31	3995.27±0.23	4035.94±0.27	4074.95±0.38	4114.70±0.32	4153.63±0.41	4191.91±0.39
24	3967.99±0.27	4010.14±0.47	4052.85±0.50	4094.33±0.59	4137.83±0.46	4178.11±0.44	4218.81±0.49	4257.18±0.47	4296.41±0.48	-
25	4106.83±0.52	4151.63±0.42	4193.62±0.50	4236.11±0.52	4277.13±0.68	-	-	-	-	-
26	4247.68±0.39	4291.04±0.66	4334.28±0.53	-	-	-	-	-	-	-

TABLE 1—*Continued*

SOLAR OSCILLATION FREQUENCIES[a]

$n \backslash l$	20	21	22	23	24	25	26	27	28	29
2	-	-	-	-	-	-	-	1104.32±0.03	1119.95±0.03	1135.18±0.02
3	1193.60±0.03	1213.63±0.02	1233.10±0.02	1252.26±0.02	1270.99±0.02	1289.41±0.02	1307.52±0.03	1325.23±0.02	1342.64±0.03	1359.74±0.02
4	1386.46±0.03	1408.06±0.01	1429.12±0.01	1449.68±0.02	1469.76±0.01	1489.44±0.01	1508.70±0.01	1527.56±0.01	1546.06±0.02	1564.16±0.02
5	1566.55±0.02	1589.26±0.01	1611.33±0.02	1632.79±0.01	1653.71±0.01	1674.09±0.02	1694.06±0.02	1713.58±0.02	1732.74±0.02	1751.59±0.02
6	1734.19±0.02	1758.25±0.02	1781.57±0.02	1804.14±0.03	1826.32±0.02	1847.91±0.02	1869.03±0.03	1889.79±0.03	1910.18±0.03	1930.22±0.02
7	1893.97±0.02	1919.85±0.03	1945.07±0.02	1969.62±0.03	1993.53±0.03	2016.94±0.03	2039.78±0.03	2062.07±0.03	2083.92±0.03	2105.39±0.03
8	2050.02±0.03	2077.72±0.03	2104.77±0.03	2131.13±0.04	2156.77±0.04	2181.78±0.04	2206.12±0.03	2229.73±0.03	2252.80±0.03	2275.34±0.03
9	2203.18±0.03	2231.86±0.03	2260.00±0.03	2287.47±0.04	2314.34±0.03	2340.50±0.04	2366.11±0.04	2390.97±0.03	2415.28±0.03	2439.02±0.03
10	2352.42±0.04	2381.90±0.04	2410.84±0.04	2439.15±0.03	2467.06±0.03	2494.35±0.03	2521.21±0.03	2547.52±0.03	2573.33±0.04	2598.67±0.03
11	2498.98±0.03	2529.34±0.03	2559.16±0.03	2588.62±0.04	2617.63±0.03	2646.24±0.04	2674.33±0.03	2702.04±0.03	2729.26±0.03	2756.11±0.03
12	2644.88±0.04	2676.14±0.05	2707.09±0.03	2737.57±0.04	2767.67±0.03	2797.28±0.04	2826.50±0.03	2855.32±0.03	2883.65±0.03	2911.56±0.03
13	2790.69±0.04	2822.95±0.05	2854.70±0.04	2886.04±0.04	2916.92±0.03	2947.35±0.03	2977.33±0.04	3007.00±0.03	3036.18±0.03	3064.97±0.04
14	2935.91±0.04	2968.88±0.04	3001.39±0.04	3033.43±0.04	3064.99±0.03	3096.17±0.04	3126.81±0.03	3157.15±0.03	3187.13±0.03	3216.64±0.03
15	3080.45±0.04	3113.92±0.03	3146.98±0.05	3179.62±0.04	3211.96±0.04	3243.80±0.04	3275.31±0.04	3306.46±0.04	3337.23±0.04	3367.57±0.04
16	3224.39±0.04	3258.46±0.04	3292.10±0.04	3325.45±0.04	3358.36±0.03	3390.93±0.04	3423.33±0.04	3455.07±0.05	3486.66±0.06	3517.84±0.06
17	3367.99±0.05	3402.83±0.04	3437.13±0.05	3471.06±0.05	3504.74±0.04	3537.87±0.05	3570.93±0.06	3603.55±0.07	3635.76±0.07	3667.60±0.07
18	3511.84±0.05	3546.93±0.05	3582.15±0.06	3616.54±0.06	3651.12±0.08	3684.81±0.07	3718.10±0.09	3751.69±0.09	3784.33±0.13	3817.01±0.13
19	3655.63±0.07	3691.54±0.09	3727.06±0.09	3762.31±0.10	3796.92±0.10	3831.46±0.14	3865.24±0.17	3899.34±0.16	3932.08±0.18	3965.58±0.21
20	3799.38±0.14	3836.00±0.19	3871.90±0.15	3907.53±0.18	3942.75±0.17	3977.49±0.24	4011.81±0.24	4046.49±0.31	4080.19±0.44	4113.96±0.41
21	3942.64±0.23	3979.67±0.22	4015.93±0.27	4052.50±0.37	4087.88±0.35	4123.56±0.41	4158.99±0.39	4193.49±0.59	4227.38±0.46	4261.50±0.57
22	4087.28±0.40	4124.63±0.32	4160.27±0.51	4197.20±0.47	4233.05±0.51	4270.76±0.56	-	-	-	-
23	4230.46±0.45	4269.51±0.60	4303.78±0.67	-	-	-	-	-	-	-

$n \backslash l$	30	31	32	33	34	35	36	37	38	39
2	1150.20±0.02	1164.97±0.02	1179.48±0.02	1193.83±0.02	1208.02±0.02	1221.92±0.03	1235.63±0.02	1249.19±0.02	1262.57±0.01	1275.77±0.03
3	1376.61±0.01	1393.18±0.01	1409.42±0.01	1425.40±0.02	1441.16±0.01	1456.62±0.01	1471.85±0.01	1486.81±0.01	1501.55±0.01	1516.06±0.02
4	1581.91±0.02	1599.32±0.01	1616.45±0.01	1633.26±0.01	1649.73±0.01	1665.95±0.01	1681.89±0.02	1697.62±0.01	1713.09±0.01	1728.28±0.02
5	1770.06±0.02	1788.28±0.02	1806.19±0.02	1823.85±0.02	1841.33±0.02	1858.48±0.02	1875.46±0.02	1892.28±0.03	1908.81±0.02	1925.19±0.03
6	1949.94±0.02	1969.48±0.02	1988.65±0.02	2007.64±0.02	2026.38±0.02	2044.88±0.02	2063.15±0.02	2081.11±0.02	2098.95±0.02	2116.58±0.02
7	2126.38±0.03	2147.01±0.03	2167.34±0.03	2187.35±0.03	2207.06±0.03	2226.44±0.03	2245.52±0.03	2264.33±0.02	2282.92±0.03	2301.26±0.03
8	2297.33±0.03	2318.91±0.03	2340.03±0.03	2360.81±0.03	2381.19±0.03	2401.34±0.03	2421.15±0.03	2440.68±0.03	2459.97±0.03	2479.01±0.02
9	2462.30±0.03	2484.94±0.03	2507.20±0.03	2529.09±0.02	2550.55±0.03	2571.78±0.03	2592.68±0.02	2613.31±0.03	2633.75±0.03	2653.83±0.03
10	2623.47±0.03	2647.81±0.03	2671.57±0.03	2694.98±0.03	2717.95±0.02	2740.48±0.02	2762.64±0.03	2784.52±0.03	2806.01±0.03	2827.22±0.03
11	2782.43±0.04	2808.29±0.03	2833.66±0.03	2858.53±0.03	2882.92±0.03	2906.71±0.03	2930.21±0.03	2953.20±0.02	2975.86±0.02	2998.07±0.02
12	2939.01±0.03	2966.09±0.03	2992.64±0.03	3018.72±0.03	3044.32±0.04	3069.52±0.03	3094.20±0.03	3118.44±0.03	3142.22±0.03	3165.68±0.03
13	3093.32±0.03	3121.17±0.03	3148.84±0.03	3175.92±0.03	3202.72±0.03	3229.07±0.03	3255.00±0.03	3280.58±0.03	3305.58±0.03	3330.30±0.03
14	3245.85±0.04	3274.74±0.04	3303.21±0.03	3331.32±0.03	3359.14±0.04	3386.55±0.04	3413.50±0.04	3440.33±0.04	3466.66±0.05	3492.53±0.04
15	3397.57±0.04	3427.36±0.04	3456.61±0.05	3485.64±0.04	3514.35±0.05	3542.63±0.05	3570.81±0.06	3598.34±0.06	3625.81±0.07	3652.81±0.09
16	3548.76±0.06	3579.18±0.07	3609.36±0.07	3638.98±0.08	3668.65±0.08	3697.86±0.09	3726.59±0.11	3755.23±0.14	3783.21±0.16	3811.26±0.15
17	3699.12±0.09	3730.41±0.08	3761.33±0.11	3791.71±0.11	3821.99±0.15	3852.03±0.14	3880.85±0.19	3911.30±0.26	3939.17±0.20	3967.92±0.26
18	3849.22±0.15	3880.58±0.16	3912.05±0.18	3943.94±0.22	3974.68±0.22	4005.31±0.26	4034.75±0.42	4064.71±0.50	4094.75±0.64	4123.31±0.50
19	3998.33±0.35	4031.38±0.31	4063.50±0.31	4094.22±0.41	4126.63±0.57	4156.53±0.48	4187.88±0.74	4219.05±0.67	4247.73±3.07	4275.13±3.07
20	4146.93±0.39	4179.99±0.57	4211.57±0.73	4246.13±0.60	4276.81±0.63	4311.30±2.31	4341.87±1.98	4370.18±1.65	4405.77±1.65	4433.82±1.65
21	4296.11±0.99	4328.79±0.84	-	-	-	-	-	-	-	-

TABLE 1—*Continued*

SOLAR OSCILLATION FREQUENCIES[a]

$n \backslash l$	40	41	42	43	44	45	46	47	48	49
1	-	-	-	1041.70±0.03	1051.90±0.03	1062.00±0.02	1072.00±0.02	1081.85±0.02	1091.60±0.02	1101.25±0.02
2	1288.72±0.02	1301.58±0.02	1314.22±0.02	1326.68±0.04	1339.09±0.03	1351.27±0.02	1363.28±0.01	1375.17±0.03	1386.93±0.02	1398.57±0.03
3	1530.32±0.01	1544.36±0.01	1558.19±0.03	1571.81±0.01	1585.19±0.01	1598.43±0.01	1611.43±0.01	1624.22±0.02	1636.92±0.03	1649.36±0.02
4	1743.29±0.02	1758.08±0.02	1772.64±0.03	1787.01±0.02	1801.25±0.02	1815.30±0.03	1829.19±0.04	1842.96±0.03	1856.50±0.03	1869.94±0.03
5	1941.44±0.03	1957.50±0.02	1973.39±0.02	1989.02±0.03	2004.62±0.02	2020.01±0.02	2035.22±0.03	2050.35±0.02	2065.29±0.03	2080.06±0.02
6	2133.93±0.02	2151.12±0.02	2168.12±0.02	2184.87±0.02	2201.41±0.03	2217.79±0.03	2233.94±0.03	2249.93±0.03	2265.69±0.02	2281.33±0.02
7	2319.35±0.02	2337.15±0.02	2354.76±0.02	2372.21±0.02	2389.40±0.02	2406.47±0.03	2423.34±0.03	2439.90±0.02	2456.45±0.03	2472.79±0.03
8	2497.91±0.03	2516.53±0.03	2535.08±0.02	2553.33±0.03	2571.41±0.02	2589.39±0.02	2607.20±0.02	2624.88±0.02	2642.35±0.02	2659.74±0.03
9	2673.71±0.03	2693.42±0.02	2712.96±0.03	2732.30±0.02	2751.49±0.03	2770.45±0.02	2789.28±0.02	2807.93±0.02	2826.38±0.02	2844.73±0.02
10	2848.17±0.02	2868.88±0.03	2889.32±0.03	2909.57±0.02	2929.54±0.03	2949.36±0.02	2968.97±0.02	2988.41±0.02	3007.66±0.02	3026.68±0.03
11	3019.95±0.03	3041.54±0.02	3062.86±0.03	3083.91±0.03	3104.69±0.03	3125.27±0.03	3145.63±0.03	3165.80±0.03	3185.76±0.03	3205.54±0.03
12	3188.54±0.03	3211.24±0.03	3233.61±0.03	3255.57±0.03	3277.25±0.03	3298.72±0.03	3319.98±0.04	3341.02±0.04	3361.79±0.03	3382.38±0.04
13	3354.55±0.03	3378.37±0.03	3401.94±0.04	3425.10±0.04	3447.84±0.03	3470.29±0.04	3492.60±0.05	3514.55±0.05	3536.29±0.05	3557.71±0.06
14	3518.07±0.05	3543.17±0.05	3567.92±0.07	3592.30±0.07	3616.18±0.06	3639.81±0.07	3663.15±0.08	3686.19±0.09	3708.96±0.07	3731.32±0.11
15	3679.32±0.09	3705.69±0.10	3731.52±0.10	3757.15±0.11	3781.97±0.12	3806.91±0.14	3831.62±0.19	3855.49±0.23	3879.34±0.31	3902.65±0.25
16	3838.65±0.17	3866.30±0.18	3893.19±0.24	3919.71±0.33	3945.72±0.36	3972.33±0.47	3997.72±0.43	4022.03±0.47	4047.14±0.48	4071.56±0.39
17	3996.13±0.32	4025.16±0.29	4052.78±0.28	4079.04±0.46	4107.16±0.36	4133.19±0.38	4160.43±0.58	4187.10±0.52	4211.93±0.52	4237.79±0.48
18	4152.74±0.59	4181.72±0.53	4209.94±1.33	4237.59±1.33	4268.52±1.13	4295.97±1.13	4321.90±1.11	4348.02±1.10	4375.47±1.07	4402.17±1.06
19	4313.06±3.07	4338.84±3.07	4365.37±3.08	4396.95±3.05	4427.33±2.79	4453.82±2.80	4481.18±2.35	4509.06±1.72	4535.71±1.77	4562.86±1.38
20	4463.63±1.65	4493.99±1.65	4526.00±1.74	4554.53±1.77	4582.86±1.59	4611.18±1.23	4639.41±1.23	4668.58±1.21	4699.30±1.15	4727.10±1.02
21	-	4652.40±3.95	4679.95±3.39	4708.25±2.82	4740.72±2.82	4767.57±2.82	4797.23±2.82	4832.08±2.82	4859.85±2.82	4888.24±2.82

$n \backslash l$	50	51	52	53	54	55	56	57	58	59
1	1110.70±0.03	1120.22±0.03	1129.50±0.03	1138.75±0.03	1147.90±0.03	1156.96±0.03	1165.85±0.03	1174.75±0.02	1183.55±0.02	1192.20±0.02
2	1409.99±0.02	1421.27±0.01	1432.42±0.01	1443.49±0.02	1454.37±0.02	1465.17±0.03	1475.80±0.02	1486.32±0.02	1496.69±0.01	1506.96±0.01
3	1661.62±0.03	1673.71±0.03	1685.68±0.02	1697.46±0.03	1709.10±0.02	1720.59±0.03	1731.99±0.02	1743.19±0.02	1754.27±0.03	1765.30±0.03
4	1883.33±0.03	1896.47±0.04	1909.55±0.04	1922.55±0.04	1935.30±0.03	1948.05±0.03	1960.65±0.03	1973.11±0.03	1985.52±0.03	1997.85±0.03
5	2094.70±0.03	2109.23±0.03	2123.52±0.03	2137.67±0.03	2151.73±0.03	2165.65±0.03	2179.36±0.03	2193.05±0.03	2206.55±0.03	2219.79±0.03
6	2296.79±0.03	2311.94±0.04	2327.08±0.03	2342.03±0.03	2356.74±0.03	2371.32±0.03	2385.78±0.03	2400.14±0.03	2414.29±0.03	2428.31±0.03
7	2488.94±0.03	2505.00±0.03	2520.92±0.04	2536.68±0.03	2552.33±0.03	2567.89±0.03	2583.29±0.03	2598.54±0.02	2613.73±0.03	2628.75±0.03
8	2676.98±0.02	2694.03±0.02	2711.03±0.03	2727.85±0.03	2744.58±0.02	2761.14±0.02	2777.55±0.02	2793.89±0.03	2810.10±0.03	2826.14±0.03
9	2862.89±0.02	2880.89±0.02	2898.75±0.02	2916.41±0.02	2933.93±0.02	2951.31±0.02	2968.61±0.02	2985.69±0.02	3002.67±0.02	3019.48±0.02
10	3045.59±0.03	3064.27±0.02	3082.86±0.03	3101.24±0.02	3119.50±0.02	3137.58±0.02	3155.55±0.02	3173.38±0.03	3191.05±0.03	3208.61±0.03
11	3225.18±0.03	3244.63±0.03	3263.92±0.04	3283.03±0.03	3302.14±0.04	3320.97±0.03	3339.68±0.04	3358.20±0.04	3376.80±0.04	3395.11±0.05
12	3402.83±0.04	3423.13±0.05	3443.23±0.05	3463.14±0.04	3482.90±0.06	3502.60±0.06	3522.21±0.07	3541.40±0.09	3560.65±0.08	3579.66±0.11
13	3578.91±0.06	3600.12±0.07	3620.96±0.10	3641.55±0.11	3662.13±0.10	3682.70±0.14	3702.70±0.16	3722.97±0.27	3743.08±0.19	3762.00±0.24
14	3753.12±0.14	3775.12±0.15	3797.19±0.17	3818.39±0.24	3839.39±0.22	3860.67±0.22	3881.14±0.24	3902.85±0.35	3921.73±0.43	3942.57±0.48
15	3925.87±0.27	3948.22±0.30	3971.03±0.26	3994.21±0.53	4014.27±0.51	4035.62±0.49	4058.07±0.47	4080.05±0.50	4101.05±0.50	4121.76±0.52
16	4095.93±0.27	4119.68±0.27	4142.89±0.16	4165.96±0.16	4188.54±0.15	4210.91±0.15	4233.57±0.17	4255.84±0.17	4277.63±0.19	4299.25±0.22
17	4263.37±0.48	4287.90±0.45	4312.23±0.42	4336.02±0.42	4360.16±0.35	4383.78±0.32	4406.49±0.34	4429.81±0.36	4452.84±0.42	4475.18±0.47
18	4428.00±0.94	4453.94±0.84	4479.53±0.75	4504.43±0.74	4529.00±0.65	4554.33±0.64	4578.98±0.62	4601.48±0.62	4625.44±0.71	4649.62±0.74
19	4591.81±1.40	4619.70±1.20	4644.89±1.27	4670.02±1.28	4697.85±1.33	4722.07±1.31	4746.57±1.26	4771.09±1.30	4797.67±1.20	4822.25±1.21
20	4753.20±1.01	4781.10±1.01	4808.20±1.12	4835.66±1.09	4861.18±1.09	4887.88±1.09	4915.49±1.09	4941.91±1.09	4969.82±1.31	4993.84±1.52
21	4912.76±2.82	4940.37±2.82	4974.22±3.39	4996.51±3.95	-	-	-	-	-	-

TABLE 1—*Continued*

SOLAR OSCILLATION FREQUENCIES[a]

$n \backslash l$	60	61	62	63	64	65	66	67	68	69
1	1200.83±0.02	1209.35±0.02	1217.85±0.02	1226.25±0.02	1234.52±0.02	1242.80±0.02	1250.94±0.02	1259.05±0.02	1267.10±0.02	1275.00±0.02
2	1517.10±0.04	1527.11±0.02	1537.01±0.02	1546.81±0.02	1556.49±0.02	1566.07±0.03	1575.46±0.02	1584.80±0.03	1594.04±0.01	1603.16±0.02
3	1776.02±0.04	1786.87±0.04	1797.45±0.05	1807.96±0.03	1818.44±0.04	1828.81±0.04	1838.96±0.04	1849.08±0.05	1859.16±0.05	1869.17±0.04
4	2010.02±0.03	2022.11±0.02	2034.10±0.03	2045.97±0.02	2057.78±0.02	2069.46±0.02	2081.11±0.02	2092.66±0.02	2104.09±0.02	2115.42±0.02
5	2233.07±0.03	2246.15±0.03	2259.03±0.02	2271.79±0.03	2284.51±0.02	2297.06±0.02	2309.49±0.02	2321.85±0.02	2334.02±0.02	2346.09±0.02
6	2442.18±0.03	2456.02±0.03	2469.74±0.03	2483.26±0.02	2496.69±0.03	2510.05±0.02	2523.30±0.02	2536.50±0.03	2549.57±0.03	2562.49±0.02
7	2643.77±0.03	2658.59±0.03	2673.36±0.03	2687.97±0.03	2702.52±0.03	2716.98±0.03	2731.41±0.03	2745.58±0.03	2759.72±0.03	2773.81±0.03
8	2842.09±0.02	2857.88±0.03	2873.60±0.02	2889.16±0.02	2904.60±0.03	2919.98±0.03	2935.18±0.03	2950.28±0.03	2965.27±0.03	2980.24±0.03
9	3036.18±0.03	3052.75±0.02	3069.22±0.03	3085.54±0.03	3101.73±0.03	3117.85±0.02	3133.76±0.03	3149.61±0.03	3165.35±0.03	3180.97±0.03
10	3226.07±0.03	3243.37±0.03	3260.61±0.03	3277.72±0.03	3294.66±0.03	3311.53±0.04	3328.26±0.04	3345.00±0.04	3361.41±0.05	3377.92±0.05
11	3413.39±0.06	3431.59±0.05	3449.45±0.06	3467.33±0.06	3484.92±0.07	3502.71±0.09	3520.26±0.09	3537.57±0.11	3555.07±0.10	3571.85±0.12
12	3598.75±0.12	3617.41±0.13	3636.40±0.16	3655.00±0.13	3673.34±0.15	3691.97±0.22	3709.86±0.22	3728.08±0.21	3746.01±0.23	3763.17±0.29
13	3782.15±0.21	3801.40±0.23	3821.55±0.44	3840.00±0.46	3859.50±0.26	3877.53±0.21	3896.12±0.19	3914.87±0.20	3933.66±0.18	3952.27±0.20
14	3963.53±0.48	3983.96±0.50	4003.39±0.52	4022.67±0.51	4042.74±0.52	4062.68±0.49	4081.75±0.49	4100.45±0.47	4119.57±0.42	4139.20±0.42
15	4142.62±0.52	4163.31±0.53	4183.72±0.48	4204.04±0.49	4224.90±0.47	4245.95±0.47	4265.93±0.47	4285.28±0.49	4305.29±0.48	4325.63±0.48
16	4320.85±0.23	4342.39±0.26	4363.80±0.26	4384.82±0.26	4405.61±0.29	4426.60±0.30	4447.82±0.31	4468.53±0.32	4488.62±0.33	4508.34±0.33
17	4497.65±0.49	4520.21±0.54	4541.55±0.53	4563.35±0.54	4585.86±0.56	4607.04±0.56	4627.38±0.56	4648.44±0.59	4670.09±0.60	4691.65±0.59
18	4673.44±0.82	4695.83±0.95	4718.44±0.99	4740.75±1.00	4762.39±0.96	4785.12±0.94	4808.77±0.94	4831.07±0.91	4850.71±0.92	4871.92±0.92
19	4844.77±1.11	4869.56±0.98	4893.82±0.98	4915.71±0.98	4940.46±0.98	4963.85±0.98	4985.25±1.18	5007.53±1.38	-	-

$n \backslash l$	70	71	72	73	74	75	76	77	78	79
1	1282.90±0.02	1290.73±0.02	1298.49±0.02	1306.20±0.01	1313.80±0.02	1321.43±0.02	1328.96±0.01	1336.42±0.02	1343.85±0.02	1351.15±0.02
2	1612.18±0.01	1621.09±0.03	1629.92±0.02	1638.60±0.02	1647.26±0.03	1655.77±0.02	1664.20±0.03	1672.54±0.02	1680.80±0.02	1688.95±0.02
3	1879.05±0.04	1888.86±0.04	1898.62±0.05	1908.24±0.04	1917.89±0.03	1927.45±0.04	1936.85±0.04	1946.22±0.04	1955.63±0.03	1964.88±0.04
4	2126.61±0.02	2137.76±0.02	2148.82±0.02	2159.78±0.02	2170.63±0.02	2181.39±0.02	2192.05±0.02	2202.62±0.02	2213.11±0.02	2223.56±0.02
5	2358.08±0.02	2369.94±0.02	2381.67±0.02	2393.36±0.02	2404.93±0.02	2416.37±0.02	2427.76±0.02	2439.09±0.02	2450.29±0.02	2461.41±0.02
6	2575.35±0.02	2588.22±0.03	2600.99±0.02	2613.64±0.02	2626.29±0.02	2638.73±0.02	2651.15±0.02	2663.51±0.02	2675.73±0.02	2687.95±0.02
7	2787.78±0.03	2801.62±0.03	2815.42±0.03	2829.09±0.03	2842.75±0.03	2856.19±0.02	2869.67±0.02	2882.95±0.02	2896.19±0.02	2909.29±0.02
8	2995.02±0.03	3009.71±0.03	3024.27±0.03	3038.72±0.03	3053.08±0.03	3067.43±0.03	3081.54±0.03	3095.69±0.03	3109.64±0.03	3123.59±0.03
9	3196.57±0.03	3211.99±0.04	3227.33±0.04	3242.52±0.04	3257.69±0.03	3272.72±0.04	3287.81±0.04	3302.59±0.04	3317.38±0.04	3332.01±0.04
10	3394.32±0.05	3410.43±0.06	3426.65±0.07	3442.69±0.07	3458.65±0.07	3474.37±0.07	3490.14±0.08	3505.99±0.08	3521.71±0.09	3537.08±0.08
11	3589.33±0.16	3606.26±0.14	3622.85±0.15	3639.85±0.16	3656.53±0.15	3673.30±0.22	3689.48±0.17	3706.38±0.18	3722.49±0.16	3738.47±0.22
12	3781.67±0.28	3799.58±0.31	3816.68±0.23	3833.96±0.35	3852.16±0.40	3868.91±0.20	3885.75±0.20	3902.44±0.20	3919.43±0.19	3936.48±0.19
13	3970.88±0.21	3989.55±0.21	4007.78±0.26	4025.60±0.25	4043.61±0.30	4061.64±0.31	4079.18±0.32	4096.42±0.33	4113.88±0.32	4131.82±0.32
14	4158.73±0.35	4177.70±0.35	4196.38±0.28	4215.03±0.27	4233.70±0.23	4252.25±0.19	4270.78±0.22	4289.32±0.19	4307.60±0.25	4325.58±0.25
15	4345.39±0.45	4364.40±0.47	4383.11±0.43	4401.98±0.41	4421.34±0.38	4440.84±0.36	4460.27±0.35	4479.58±0.30	4498.22±0.31	4516.21±0.30
16	4528.19±0.34	4548.40±0.34	4569.02±0.33	4589.24±0.37	4608.95±0.38	4628.75±0.44	4648.68±0.46	4668.23±0.56	4687.16±0.56	4705.98±0.67
17	4712.45±0.60	4732.55±0.55	4752.51±0.52	4772.57±0.52	4793.03±0.53	4814.53±0.54	4835.36±0.57	4855.32±0.57	4875.36±0.58	4894.83±0.58
18	4894.18±0.92	4916.21±0.92	4937.66±0.92	4958.84±0.92	4979.32±1.11	4999.33±1.29	-	-	-	-

TABLE 1—*Continued*

SOLAR OSCILLATION FREQUENCIES[a]

$n \backslash l$	80	81	82	83	84	85	86	87	88	89
1	1358.45±0.01	1365.70±0.02	1372.91±0.02	1380.06±0.02	1387.08±0.02	1394.10±0.02	1401.13±0.03	1408.00±0.02	1414.89±0.02	1421.77±0.02
2	1697.06±0.02	1705.09±0.02	1712.98±0.03	1720.79±0.03	1728.61±0.02	1736.29±0.03	1743.86±0.03	1751.44±0.03	1758.95±0.03	1766.36±0.03
3	1974.08±0.04	1983.25±0.04	1992.44±0.04	2001.43±0.04	2010.41±0.04	2019.36±0.03	2028.30±0.04	2037.00±0.04	2045.79±0.04	2054.43±0.04
4	2233.88±0.02	2244.05±0.03	2254.19±0.02	2264.24±0.02	2274.20±0.03	2284.18±0.03	2294.04±0.04	2303.70±0.04	2313.33±0.03	2322.93±0.04
5	2472.46±0.02	2483.41±0.02	2494.31±0.02	2505.12±0.02	2515.87±0.02	2526.54±0.02	2537.16±0.02	2547.74±0.02	2558.19±0.02	2568.61±0.02
6	2700.11±0.02	2712.17±0.02	2724.15±0.02	2736.08±0.02	2747.95±0.02	2759.73±0.02	2771.43±0.02	2783.06±0.02	2794.69±0.02	2806.22±0.02
7	2922.32±0.02	2935.38±0.02	2948.26±0.02	2961.06±0.02	2973.86±0.02	2986.43±0.02	2998.99±0.02	3011.48±0.02	3023.81±0.02	3036.17±0.02
8	3137.35±0.03	3151.11±0.03	3164.74±0.03	3178.33±0.02	3191.76±0.03	3205.21±0.03	3218.52±0.03	3231.75±0.03	3244.96±0.02	3258.10±0.03
9	3346.76±0.04	3361.32±0.04	3375.73±0.04	3390.11±0.04	3404.35±0.04	3418.69±0.05	3432.75±0.05	3446.90±0.05	3460.90±0.04	3474.94±0.04
10	3552.45±0.09	3567.94±0.09	3582.86±0.09	3598.20±0.09	3613.35±0.13	3628.19±0.11	3643.25±0.13	3657.86±0.12	3672.89±0.14	3687.70±0.14
11	3754.55±0.16	3770.62±0.21	3786.72±0.23	3802.19±0.24	3818.75±0.28	3834.50±0.34	3850.12±0.24	3865.47±0.29	3881.02±0.28	3895.73±0.23
12	3953.28±0.17	3969.94±0.17	3986.57±0.12	4003.04±0.13	4019.39±0.10	4035.67±0.12	4051.87±0.12	4068.07±0.15	4084.26±0.16	4100.50±0.17
13	4149.76±0.31	4166.99±0.32	4183.77±0.32	4200.74±0.33	4217.95±0.36	4235.10±0.33	4252.15±0.37	4269.17±0.34	4285.84±0.35	4301.97±0.38
14	4343.39±0.28	4361.15±0.29	4379.16±0.31	4397.50±0.33	4415.69±0.34	4433.04±0.38	4450.01±0.38	4467.37±0.40	4484.75±0.40	4501.66±0.38
15	4534.19±0.30	4552.67±0.30	4571.43±0.33	4590.24±0.33	4609.04±0.33	4627.30±0.30	4645.46±0.36	4663.98±0.35	4682.36±0.43	4699.95±0.50
16	4725.56±0.67	4744.33±0.70	4762.24±0.76	4780.62±0.77	4800.41±0.79	4820.12±0.78	4838.30±0.77	4856.49±0.76	4875.29±0.73	4895.16±0.73
17	4914.96±0.58	4935.74±0.58	4956.79±0.58	4976.03±0.70	4993.89±0.82	-	-	-	-	-

$n \backslash l$	90	91	92	93	94	95	96	97	98	99
1	1428.51±0.01	1435.26±0.02	1441.98±0.02	1448.56±0.04	1455.17±0.02	1461.75±0.04	1468.20±0.03	1474.68±0.04	1481.07±0.03	1487.40±0.03
2	1773.68±0.04	1780.99±0.05	1788.26±0.04	1795.37±0.05	1802.46±0.04	1809.61±0.05	1816.57±0.05	1823.49±0.05	1830.43±0.06	1837.19±0.05
3	2063.23±0.04	2071.86±0.05	2080.26±0.05	2088.85±0.05	2097.30±0.04	2105.66±0.05	2114.04±0.05	2122.26±0.05	2130.59±0.05	2138.69±0.04
4	2332.39±0.04	2341.87±0.04	2351.12±0.04	2360.34±0.04	2369.65±0.04	2378.72±0.05	2387.88±0.06	2396.87±0.05	2405.87±0.04	2414.64±0.06
5	2579.00±0.02	2589.32±0.02	2599.56±0.02	2609.71±0.03	2619.93±0.03	2630.04±0.03	2640.09±0.03	2650.01±0.03	2660.08±0.04	2669.85±0.04
6	2817.65±0.02	2829.04±0.02	2840.38±0.02	2851.64±0.02	2862.84±0.02	2873.99±0.02	2885.01±0.02	2895.98±0.02	2906.92±0.02	2917.84±0.02
7	3048.46±0.02	3060.65±0.02	3072.75±0.02	3084.79±0.02	3096.76±0.02	3108.61±0.02	3120.45±0.02	3132.22±0.02	3143.89±0.02	3155.54±0.02
8	3271.19±0.03	3284.10±0.03	3297.02±0.03	3309.87±0.03	3322.54±0.02	3335.31±0.03	3347.92±0.03	3360.55±0.03	3373.04±0.03	3385.53±0.03
9	3488.68±0.04	3502.52±0.06	3516.24±0.06	3529.94±0.07	3543.59±0.06	3556.98±0.06	3570.51±0.07	3583.80±0.08	3597.08±0.08	3610.54±0.09
10	3702.27±0.16	3716.76±0.14	3730.87±0.14	3745.68±0.16	3759.88±0.17	3774.38±0.19	3788.46±0.15	3802.41±0.20	3816.48±0.21	3830.49±0.26
11	3910.56±0.30	3925.58±0.23	3940.55±0.20	3956.02±0.21	3971.37±0.20	3986.31±0.22	4001.25±0.21	4016.13±0.21	4030.71±0.22	4045.23±0.19
12	4116.50±0.17	4132.21±0.17	4148.18±0.17	4164.28±0.18	4179.88±0.17	4195.16±0.18	4210.56±0.17	4226.05±0.17	4241.34±0.15	4256.60±0.14
13	4318.52±0.37	4335.63±0.38	4352.27±0.39	4368.28±0.39	4384.03±0.39	4400.13±0.39	4416.73±0.37	4433.24±0.35	4449.27±0.35	4464.91±0.32
14	4518.24±0.39	4535.09±0.34	4552.69±0.34	4570.30±0.31	4587.44±0.31	4604.22±0.30	4621.04±0.28	4638.00±0.28	4654.84±0.21	4671.48±0.27
15	4717.14±0.51	4734.57±0.56	4751.87±0.57	4768.45±0.58	4784.71±0.66	4802.15±0.65	4820.67±0.71	4838.86±0.72	4856.26±0.74	4873.66±0.74
16	4915.67±0.73	4934.77±0.73	4953.29±0.73	4970.70±0.88	4987.36±1.03	-	-	-	-	-

$n \backslash l$	100	101	102	103	104	105	106	107	108	109
1	1493.74±0.03	1499.94±0.04	1506.28±0.02	1512.47±0.05	1518.61±0.02	1524.64±0.06	1530.75±0.04	1536.74±0.06	1542.76±0.05	1548.65±0.05
2	1844.12±0.04	1850.76±0.04	1857.45±0.04	1864.12±0.04	1870.70±0.04	1877.22±0.03	1883.82±0.04	1890.22±0.03	1896.71±0.03	1903.13±0.03
3	2146.94±0.05	2154.86±0.05	2163.02±0.04	2170.88±0.05	2178.80±0.05	2186.81±0.06	2194.53±0.04	2202.29±0.04	2210.08±0.06	2217.74±0.06
4	2423.47±0.05	2432.19±0.06	2440.89±0.07	2449.57±0.07	2458.08±0.06	2466.65±0.08	2475.06±0.07	2483.54±0.09	2492.01±0.08	2500.29±0.06
5	2679.68±0.03	2689.55±0.03	2699.42±0.04	2708.97±0.04	2718.57±0.03	2728.32±0.04	2737.85±0.04	2747.36±0.04	2756.90±0.05	2766.36±0.05
6	2928.67±0.03	2939.42±0.02	2950.15±0.02	2960.73±0.03	2971.26±0.03	2981.79±0.03	2992.23±0.03	3002.66±0.03	3013.00±0.02	3023.27±0.02
7	3167.17±0.02	3178.71±0.02	3190.14±0.02	3201.50±0.02	3212.83±0.03	3224.11±0.03	3235.34±0.03	3246.52±0.03	3257.64±0.03	3268.74±0.03
8	3397.96±0.04	3410.22±0.04	3422.46±0.04	3434.90±0.04	3447.08±0.04	3459.21±0.04	3471.18±0.05	3483.12±0.05	3495.14±0.05	3507.11±0.05
9	3623.84±0.07	3636.81±0.08	3649.78±0.09	3662.67±0.10	3675.57±0.10	3688.65±0.10	3701.66±0.10	3714.34±0.12	3727.02±0.15	3739.74±0.15
10	3844.40±0.15	3858.03±0.24	3871.92±0.25	3885.47±0.20	3899.32±0.34	3912.92±0.24	3926.54±0.23	3939.94±0.21	3952.95±0.22	3966.11±0.28
11	4059.87±0.20	4074.44±0.20	4088.71±0.20	4102.67±0.20	4116.85±0.20	4131.38±0.20	4145.93±0.21	4160.21±0.24	4174.19±0.25	4188.06±0.25
12	4271.92±0.14	4287.07±0.12	4301.95±0.13	4316.90±0.14	4331.81±0.16	4346.54±0.16	4361.32±0.21	4376.35±0.22	4391.40±0.25	4406.20±0.34
13	4480.43±0.33	4496.17±0.31	4512.08±0.29	4527.82±0.29	4543.15±0.27	4558.29±0.26	4573.79±0.30	4589.71±0.35	4605.49±0.35	4620.84±0.53
14	4688.09±0.31	4704.24±0.33	4719.84±0.34	4735.17±0.33	4750.21±0.37	4765.33±0.44	4781.22±0.47	4798.33±0.48	4814.80±0.48	4831.53±0.48
15	4891.44±0.75	4910.30±0.75	4929.38±0.75	4946.77±0.75	4962.94±0.75	4978.63±0.90	4993.98±1.05	-	-	-

TABLE 1—*Continued*

SOLAR OSCILLATION FREQUENCIES[a]

n \ l	110	112	114	116	118	120	122	124	126	128
1	1554.51±0.05	1566.09±0.05	1577.76±0.05	1589.05±0.04	1600.20±0.05	1611.37±0.06	1622.29±0.05	1633.18±0.07	1644.05±0.05	1654.66±0.07
2	1909.46±0.03	1922.14±0.03	1934.67±0.04	1946.99±0.03	1959.30±0.04	1971.45±0.03	1983.51±0.03	1995.36±0.04	2007.18±0.03	2018.93±0.04
3	2225.24±0.06	2240.50±0.07	2255.35±0.08	2270.06±0.09	2284.63±0.07	2298.85±0.08	2312.92±0.08	2326.82±0.07	2340.40±0.06	2354.08±0.07
4	2508.42±0.07	2524.89±0.06	2541.21±0.07	2557.41±0.08	2573.33±0.09	2589.02±0.07	2604.74±0.12	2620.34±0.11	2635.62±0.10	2651.10±0.11
5	2775.73±0.04	2794.43±0.04	2812.93±0.05	2831.17±0.05	2849.30±0.05	2867.31±0.06	2885.01±0.06	2902.74±0.06	2919.98±0.09	2937.28±0.07
6	3033.48±0.02	3053.74±0.03	3073.86±0.03	3093.78±0.04	3113.38±0.03	3132.89±0.04	3152.10±0.04	3171.24±0.05	3190.14±0.04	3208.85±0.06
7	3279.71±0.03	3301.57±0.03	3323.40±0.04	3344.82±0.04	3366.11±0.05	3387.22±0.05	3408.27±0.05	3428.96±0.06	3449.63±0.06	3470.00±0.06
8	3518.90±0.06	3542.54±0.05	3565.82±0.06	3588.97±0.07	3611.97±0.07	3634.64±0.09	3657.30±0.09	3679.61±0.12	3701.99±0.15	3723.62±0.15
9	3752.46±0.17	3777.33±0.17	3802.18±0.13	3826.71±0.20	3851.48±0.23	3875.55±0.21	3898.94±0.22	3923.24±0.32	3946.20±0.30	3969.00±0.16
10	3979.28±0.32	4005.64±0.34	4032.12±0.35	4057.75±0.38	4083.05±0.38	4108.62±0.39	4134.39±0.39	4159.81±0.39	4183.88±0.40	4208.38±0.38
11	4201.92±0.26	4229.60±0.27	4257.44±0.28	4284.70±0.28	4311.06±0.28	4338.08±0.28	4364.54±0.28	4391.51±0.29	4417.72±0.30	4443.19±0.30
12	4420.56±0.34	4449.66±0.34	4478.62±0.35	4506.68±0.35	4534.27±0.37	4562.14±0.41	4590.93±0.43	4619.21±0.45	4647.25±0.47	4674.52±0.45
13	4636.11±0.56	4666.44±0.56	4696.52±0.55	4725.49±0.57	4753.46±0.59	4781.44±0.59	4811.24±0.59	4841.95±0.59	4872.64±0.59	4902.43±0.59
14	4847.97±0.48	4882.36±0.48	4913.93±0.48	4946.07±0.57	4975.54±0.67	-	-	-	-	-

n \ l	130	132	134	136	138	140	145	150	155	160
1	1664.81±0.07	1674.94±0.08	1685.33±0.07	1695.25±0.10	1705.38±0.13	1715.50±0.14	-	-	-	-
2	2030.62±0.03	2042.15±0.04	2053.63±0.04	2065.02±0.05	2076.28±0.06	2087.32±0.06	-	2148.50±1.35	2169.27±1.39	2195.28±1.69
3	2367.50±0.06	2380.76±0.06	2393.70±0.07	2406.63±0.06	2419.33±0.06	2431.92±0.06	2462.83±0.85	2494.98±0.65	2523.10±0.61	2553.13±0.58
4	2666.20±0.11	2681.25±0.12	2696.28±0.13	2710.92±0.13	2725.88±0.14	2740.62±0.16	2776.95±0.40	2811.51±0.43	2846.28±0.38	2880.28±0.36
5	2954.43±0.08	2971.47±0.07	2988.12±0.08	3004.50±0.10	3021.14±0.09	3037.57±0.09	3076.54±0.42	3116.76±0.47	3154.74±0.43	3192.29±0.39
6	3227.40±0.07	3246.15±0.08	3264.24±0.08	3282.20±0.10	3300.14±0.13	3318.22±0.10	3361.13±0.46	3405.04±0.43	3447.29±0.42	3489.41±0.39
7	3490.28±0.08	3510.50±0.09	3530.29±0.10	3550.53±0.13	3569.78±0.14	3589.67±0.23	3637.36±0.52	3684.54±0.52	3730.01±0.57	3777.13±0.51
8	3745.60±0.18	3767.31±0.15	3789.01±0.29	3811.96±0.12	3830.19±0.29	3851.18±0.34	3903.35±0.67	3954.48±0.64	4004.46±0.74	4053.61±0.77
9	3992.17±0.16	4015.42±0.16	4038.54±0.16	4060.90±0.16	4083.03±0.20	4105.10±0.23	4161.48±0.82	4217.81±0.88	4268.98±0.99	4323.45±1.34
10	4233.02±0.38	4257.81±0.38	4282.13±0.38	4305.93±0.38	4329.41±0.46	4352.55±0.54	4416.43±1.15	4475.10±1.25	4530.32±1.19	4586.86±1.45
11	4468.85±0.30	4494.46±0.30	4519.58±0.30	4545.14±0.30	4569.95±0.36	4595.54±0.41	4661.48±1.25	-	-	-
12	4700.93±0.45	4726.92±0.45	4751.64±0.45	4777.35±0.45	4804.63±0.54	4831.80±0.63	-	-	-	-
13	4932.69±0.59	4959.75±0.71	4985.51±0.82	-	-	-	-	-	-	-

n \ l	165	170	175	180	185	190	195	200	205	210	215
1	-	-	-	1900.4±7.0	-	-	-	1975.1±7.0	-	-	-
2	2222.9±1.6	2250.6±1.5	2274.4±1.4	2302.3±1.5	2324.1±1.6	2344.1±1.2	2371.1±1.2	2395.6±1.0	2415.3±1.0	2438.4±0.7	2460.3±0.6
3	2580.2±0.5	2607.5±0.5	2634.7±0.4	2660.6±0.4	2687.3±0.4	2713.6±0.3	2739.4±0.4	2766.0±0.4	2791.7±0.4	2816.4±0.4	2841.2±0.4
4	2914.1±0.3	2947.0±0.4	2978.9±0.4	3010.2±0.3	3040.9±0.3	3071.5±0.3	3101.3±0.4	3130.2±0.3	3160.4±0.3	3187.9±0.4	3216.6±0.3
5	3229.6±0.4	3266.1±0.4	3301.5±0.5	3336.6±0.4	3371.5±0.4	3406.1±0.4	3439.3±0.4	3472.1±0.4	3505.7±0.4	3537.7±0.4	3569.0±0.4
6	3530.1±0.4	3571.5±0.4	3610.5±0.4	3650.2±0.4	3689.0±0.5	3727.6±0.5	3765.2±0.5	3800.2±0.5	3838.0±0.5	3873.4±0.6	3908.9±0.5
7	3821.1±0.6	3867.0±0.5	3910.4±0.5	3952.8±0.6	3994.8±0.7	4035.6±0.8	4079.2±0.8	4116.4±0.9	4155.5±0.9	4197.0±1.0	4236.4±0.9
8	4100.2±0.8	4149.6±0.8	4198.0±0.8	4244.9±0.8	4288.8±0.8	4336.9±0.8	4382.0±0.8	4425.0±0.9	4470.6±0.9	4509.8±1.1	4553.4±1.1
9	4375.1±1.4	4426.7±1.6	4476.9±2.0	4526.5±2.0	4574.6±2.0	4622.7±1.9	4673.1±2.1	-	-	-	-
10	4642.3±1.5	4695.7±1.5	-	-	-	-	-	-	-	-	-

n \ l	220	225	230	235	240	245	250	255	260	265	270
1	2044.9±7.0	-	-	-	2110.0±7.0	-	-	-	2159.9±7.0	-	-
2	2482.4±0.5	2502.9±0.4	2524.1±0.4	2543.7±0.4	2562.7±0.4	2582.0±0.4	2601.0±0.4	2620.6±0.4	2640.2±0.4	2658.3±0.4	2676.0±0.4
3	2865.1±0.3	2890.0±0.4	2914.5±0.3	2938.3±0.3	2963.6±0.3	2987.4±0.3	3010.2±0.3	3034.3±0.2	3057.0±0.2	3079.9±0.2	3102.4±0.3
4	3244.0±0.3	3270.6±0.3	3298.0±0.3	3323.9±0.3	3350.2±0.3	3376.2±0.3	3402.4±0.3	3427.4±0.4	3452.5±0.4	3478.3±0.4	3503.7±0.4
5	3600.3±0.3	3631.8±0.4	3663.1±0.4	3694.1±0.4	3724.5±0.4	3752.4±0.4	3782.8±0.5	3811.1±0.5	3840.0±0.4	3869.1±0.5	3898.1±0.5
6	3945.7±0.6	3978.5±0.7	4013.0±0.6	4048.5±0.6	4081.0±0.7	4113.6±1.0	4147.2±1.0	4179.4±1.0	4211.1±1.0	4242.6±1.0	4274.4±1.0
7	4273.3±0.9	4315.2±0.9	4350.7±0.9	4388.2±0.9	4426.2±0.8	4461.1±0.8	-	-	4533.4±17.	-	-
8	4594.8±1.1	4636.0±1.2	4674.8±1.2	4717.2±1.3	4729.4±17.	-	-	-	-	-	-

TABLE 1—*Continued*

Solar Oscillation Frequencies[a]

$n \backslash l$	275	280	285	290	295	300	305	310	315	320	325
0	-	1698.2±5.5	-	-	-	1743.6±5.5	-	-	-	1799.1±5.5	-
1	-	2232.4±1.0	2245.7±1.4	2258.8±1.4	2271.2±1.3	2291.2±1.5	2303.8±1.3	2321.3±1.3	2331.4±1.1	2343.8±0.9	2357.5±0.6
2	2693.2±0.4	2711.9±0.4	2728.6±0.4	2746.7±0.4	2763.6±0.4	2780.3±0.4	2796.5±0.3	2813.2±0.4	2829.2±0.4	2845.3±0.4	2861.6±0.3
3	3124.9±0.3	3147.4±0.3	3169.2±0.3	3190.7±0.3	3212.0±0.3	3233.7±0.3	3254.7±0.4	3275.5±0.3	3295.8±0.3	3315.8±0.3	3336.3±0.3
4	3528.3±0.4	3552.7±0.4	3577.5±0.4	3601.5±0.4	3625.8±0.4	3650.1±0.4	3673.8±0.5	3697.5±0.5	3721.8±0.5	3745.6±0.4	3769.3±0.4
5	3925.6±0.6	3954.4±0.6	3980.8±0.7	4006.6±0.7	4035.9±0.8	4061.6±0.7	4087.1±0.7	4111.6±0.6	4140.1±0.6	4164.9±0.6	4191.3±0.9
6	4306.9±0.9	4338.4±0.8	4369.3±0.9	4396.0±0.9	4427.9±1.0	4458.8±1.0	4486.0±0.7	-	-	4561.5±12.	-
7	-	4706.2±17.	-	-	-	4815.1±17.	-	-	-	4940.1±17.	-

$n \backslash l$	330	335	340	345	350	355	360	365	370	375	380
0	-	-	1867.7±5.5	-	-	-	1903.9±5.5	-	-	-	1942.3±5.5
1	2370.1±0.7	2384.6±0.7	2400.6±0.8	2413.4±0.7	2427.3±0.8	2441.1±0.9	2454.8±0.8	2464.6±1.0	2480.5±1.0	2495.9±1.0	2503.6±0.9
2	2877.3±0.4	2893.4±0.4	2909.3±0.3	2923.9±0.3	2939.5±0.3	2954.8±0.3	2970.4±0.3	2984.8±0.3	3000.2±0.3	3014.7±0.4	3030.8±0.4
3	3355.9±0.3	3375.0±0.4	3393.7±0.3	3413.4±0.4	3433.3±0.3	3451.8±0.4	3469.9±0.4	3487.8±0.3	3507.3±0.3	3524.3±0.3	3542.3±0.4
4	3792.4±0.4	3815.7±0.4	3839.2±0.6	3862.2±0.6	3883.5±0.7	3908.6±0.7	3931.1±0.7	3951.1±0.7	3975.0±0.6	3997.1±0.6	4019.4±0.6
5	4217.6±0.9	4243.5±1.1	4267.2±1.2	4292.3±1.3	4319.8±1.4	4343.2±1.3	4367.6±1.4	4390.0±1.5	4416.7±1.5	4446.4±1.5	4469.1±1.4
6	-	-	4665.0±12.	-	-	-	4760.6±12.	-	-	-	4869.2±12.
7	-	-	5062.5±17.	-	-	-	5155.6±17.	-	-	-	-

$n \backslash l$	385	390	395	400	420	440	460	480	500	520	540
0	-	-	-	1998.0±5.5	2042.8±5.5	2090.9±5.5	2147.4±5.5	2190.2±5.5	2227.8±5.5	2277.8±5.5	2325.4±5.6
1	2517.8±0.8	2532.3±0.8	2545.2±0.6	2546.7±7.0	2604.2±7.0	2657.7±6.0	2700.5±6.0	2745.3±6.0	2795.2±5.8	2846.4±5.8	2890.1±5.7
2	3046.2±0.3	3060.3±0.3	3074.4±0.3	3089.6±12.	3138.5±12.	3194.4±8.7	3252.4±8.4	3307.8±8.4	3359.1±8.2	3412.0±7.9	3471.3±7.8
3	3560.2±0.4	3577.4±0.4	3595.5±0.4	3606.5±10.	3669.2±10.	3740.6±8.3	3804.8±8.4	3861.5±8.3	3925.4±8.3	3990.8±8.3	4050.0±8.3
4	4041.7±0.7	4062.3±0.7	4082.9±0.7	4092.1±9.2	4175.3±9.2	4264.2±8.7	4334.6±8.9	4406.7±8.7	4475.4±11.	4549.0±11.	4635.9±11.
5	4492.8±1.8	4513.6±1.7	4537.7±1.7	4543.1±9.2	4641.9±9.2	4738.6±8.7	4827.5±8.9	4873.1±8.7	4967.0±11.	5080.0±11.	5126.6±11.
6	-	-	-	4974.2±12.	5065.2±12.	5172.2±12.	-	-	-	-	-

$n \backslash l$	560	580	600	620	640	660	680	700	720	740	760	780	800	820
0	2365± 6	2404± 6	2438± 4	2487± 5	2524± 4	2563± 4	2602± 4	2632± 4	2671± 4	2713± 4	2743± 4	2778± 4	2821± 4	2858± 4
1	2930± 4	2978± 4	3025± 4	3065± 4	3117± 4	3159± 4	3199± 4	3241± 4	3281± 4	3329± 4	3373± 4	3411± 4	3451± 4	3497± 4
2	3520± 6	3566± 6	3622± 5	3676± 5	3722± 5	3781± 5	3833± 6	3877± 6	3922± 6	3982± 6	4025± 6	4066± 6	4120± 7	4172± 8
3	4105± 7	4163± 6	4225± 5	4290± 5	4344± 5	4407± 6	4456± 6	4502± 7	4574± 7	4627± 7	4676± 7	4729± 7	4785± 7	4844± 7
4	4691±11	4749±11	4815±11	4882±11	4946±11	4998±11	5069±11	5124±11	5198±11	5278±11	-	-	-	-
5	5220±11	5314±11	-	-	-	-	-	-	-	-	-	-	-	-

$n \backslash l$	840	860	880	900	920	940	960	980	1000	1020	1040	1060	1080	1100
0	2891± 4	2926± 4	2957± 4	2984± 4	3022± 4	3047± 4	3078± 3	3113± 3	3140± 3	3168± 3	3196± 3	3231± 3	3261± 3	3282± 4
1	3547± 4	3586± 4	3623± 4	3664± 4	3701± 4	3751± 4	3786± 4	3830± 4	3874± 5	3911± 5	3945± 5	3997± 5	4038± 5	4070± 6
2	4225± 8	4276± 8	4320± 8	4374± 8	4425±10	4465±12	4507±13	4549±13	4601±14	4648±14	4694±16	4737±16	4806±16	4861±16
3	4899± 7	4952± 7	5009± 7	5073± 7	5115± 7	5167± 7	5200± 7	5245± 7	5311± 7	5346± 7	-	-	-	-

TABLE 1—*Continued*

SOLAR OSCILLATION FREQUENCIES[a]

$n \backslash l$	1120	1140	1160	1180	1200	1220	1240	1260	1280	1300	1320	1340	1360	1380
0	3309± 3	3342± 3	3369± 4	3395± 4	3418± 4	3445± 4	3471± 4	3494± 5	3519± 5	3540± 5	3565± 6	3602± 5	3621± 5	3644± 6
1	4108± 6	4147± 6	4189± 7	4232± 9	4267± 9	4304±10	4356±12	4391±14	4428±14	4462±14	4502±21	4537±21	4591±21	4642±22
2	4889±16	4944±16	5017±16	5075±16	5110±16	5124±16	5197±16	5244±16	5238±16	5299±16	-	-	-	-

$n \backslash l$	1400	1420	1440	1460	1480	1500	1520	1540	1560	1580	1600	1620	1640	1660
0	3676± 7	3702± 7	3711± 7	3739± 7	3771± 8	3778± 8	3815±10	3846±11	3855±14	3881±14	3907±14	3943±14	3957±14	3977±14
1	4671±23	4709±23	4767±23	4836±23	4887±23	4924±23	4957±23	4968±23	5083±23	5062±23	5082±23	5088±23	5134±23	5194±23

$n \backslash l$	1680	1700	1720	1740	1760	1780	1800	1820	1840	1860
0	3992±14	4019±14	4011±14	4042±14	4048±14	4067±14	4151±14	4140±14	4133±14	4156±14